

NATIONAL AERONAUTICS AND SPACE ADMINISTRATION

# Space Programs Summary No. 37-34, Volume VI

for the period May 1, 1965 to June 30, 1965

## Space Exploration Programs and Space Sciences

GPO PRICE \$ \_\_\_\_\_

CFSTI PRICE(S) \$ \_\_\_\_\_

Hard copy (HC) 3.00

Microfiche (MF) 50

ff 653 July 65

FACILITY FORM 602

**N 65-33878**

(ACCESSION NUMBER)

53  
(PAGES)

CR-64884  
(NASA CR OR TMX OR AD NUMBER)

(THRU)

(CODE)

DO 30  
(CATEGORY)

**jpl**

**JET PROPULSION LABORATORY**  
**CALIFORNIA INSTITUTE OF TECHNOLOGY**  
**PASADENA, CALIFORNIA**

July 31, 1965

NATIONAL AERONAUTICS AND SPACE ADMINISTRATION

*Space Programs Summary No. 37-34, Volume VI*

for the period May 1, 1965 to June 30, 1965

*Space Exploration Programs and Space Sciences*

JET PROPULSION LABORATORY  
CALIFORNIA INSTITUTE OF TECHNOLOGY  
PASADENA, CALIFORNIA

July 31, 1965

## Preface

The *Space Programs Summary* is a six-volume, bimonthly publication that documents the current project activities and supporting research and advanced development efforts conducted or managed by JPL for the NASA space exploration programs. The titles of all volumes of the *Space Programs Summary* are:

- Vol. I. The Lunar Program (Confidential)
- Vol. II. The Planetary-Interplanetary Program (Confidential)
- Vol. III. The Deep Space Network (Unclassified)
- Vol. IV. Supporting Research and Advanced Development (Unclassified)
- Vol. V. Supporting Research and Advanced Development (Confidential)
- Vol. VI. Space Exploration Programs and Space Sciences (Unclassified)

The *Space Programs Summary*, Vol. VI consists of an unclassified digest of appropriate material from Vols. I, II, and III; an original presentation of technical supporting activities, including engineering development of environmental-test facilities, and quality assurance and reliability; and a reprint of the space science instrumentation studies of Vols. I and II. This instrumentation work is conducted by the JPL Space Sciences Division and also by individuals of various colleges, universities, and other organizations. All such projects are supported by the Laboratory and are concerned with the development of instruments for use in the NASA space flight programs.



W. H. Pickering, Director  
*Jet Propulsion Laboratory*

### Space Programs Summary No. 37-34, Vol. VI

Copyright © 1965, Jet Propulsion Laboratory, California Institute of Technology  
Prepared under Contract No. NAS 7-100, National Aeronautics & Space Administration

## Contents

### LUNAR PROGRAM

<b>I. <i>Ranger</i> Project</b>	1
A. Introduction	1
B. <i>Ranger VIII</i> Trajectory Analysis	2
C. Mark II L-Band Communication System Performance During the Block III Missions	12
<b>II. <i>Surveyor</i> Project</b>	14
A. Introduction	14
B. Systems Testing	14
C. Flight Control	16
D. Electronics	17
E. Testing Facilities and Equipment	18

### PLANETARY-INTERPLANETARY PROGRAM

<b>III. <i>Mariner</i> Project</b>	19
A. Introduction	19
B. <i>Mariner IV</i> Space Flight Operations	20
C. <i>Mariner IV</i> Radio Subsystem Performance	21

### DEEP SPACE NETWORK

<b>IV. Deep Space Instrumentation Facility</b>	23
A. Introduction	23
B. Tracking Stations Engineering and Operations	23
C. Developmental and Testing Activities	26

### SUPPORTING ACTIVITIES

<b>V. Environmental Test Facilities</b>	29
A. A Preliminary Study of the Stability of a Multiple- Vibration-Exciter Control System	29
B. Special Equalization Procedure for Random Vibration Testing	32

### SPACE SCIENCES

<b>VI. Space Instruments</b>	37
A. <i>Mariner IV</i> Ionization Chamber Failure Analysis	37
B. <i>Mariner IV</i> Plasma Probe Failure Analysis	39
C. <i>Mariner IV</i> TV Interpretation Studies	41
D. Spurious TV Image Phenomena	44
<b>VII. Space Instrument Systems</b>	48
A. Space Sciences Encounter Planning Activities	48



# LUNAR PROGRAM

## I. *Ranger* Project

### A. Introduction

The *Ranger* Project was established to develop a space flight technology for transporting engineering and scientific instruments to the Moon and planets. Nine *Ranger* launchings, using *Atlas D-Agena B* vehicles, were planned; all of these flights have now been made.

*Rangers I* and *II* (Block I) were not lunar-oriented, but were engineering evaluation flights to test the basic systems to be employed in later lunar and planetary missions. Several scientific experiments were carried on a non-interference basis. Both spacecraft performed satisfactorily within the constraints of the obtained satellite orbit. *Rangers III*, *IV*, and *V* (Block II) carried a gamma-ray instrument, a TV camera, and a rough-landing seismometer capsule; each of these flights experienced failures.

The objective of the *Ranger* Block III (*Rangers VI*, *VII*, *VIII*, and *IX*) flights was to obtain pictures of the lunar surface, at least an order of magnitude better than those obtainable with Earth-based photography, which will be of benefit to both the scientific program and the U.S. manned lunar flight program. The *Ranger VI* spacecraft, which was launched from the Eastern Test Range (ETR) on January 30, 1964, and impacted the Moon essentially on target on February 2, 1964, did not accomplish the primary flight objective due to a failure of the TV subsystem to transmit pictures. An extensive analysis of the TV subsystem failure was conducted, new and reworked hardware was assembled as the *Ranger VII* TV subsystem, and extensive testing of the reassembled TV subsystem was performed.

The *Ranger VII* spacecraft was launched from the ETR on July 28, 1964, and impacted the Moon on target on

July 31, 1964. The mission flight objective was accomplished. The outstanding events of the mission were the precision of the trajectory correction and the transmission of 4304 video pictures of the lunar surface.

The *Ranger VIII* spacecraft was launched from the ETR on February 17, 1965, and impacted the Moon on target on February 20, 1965. The mission flight objective was again accomplished, and approximately 7000 high-quality video pictures of the lunar surface were transmitted from the spacecraft. The final calculated impact point represented a miss of only 15 miles from the originally selected aiming point.

The *Ranger IX* spacecraft was launched from the ETR on March 21, 1965, and impacted the Moon on target on March 24, 1965. Again, the mission flight objective was accomplished; following a successful terminal maneuver, 5814 excellent-quality video pictures of the lunar surface were transmitted from the spacecraft. The resolution of the final pictures is the best resolution obtained during any of the Block III flights. For the first time, the video signals, as relayed from the Goldstone Space Communications Station to JPL by microwave link, were scan-converted for live commercial TV transmission. The final calculated impact point of *Ranger IX* represented a miss of only 4 miles from the originally selected aiming point.

## B. *Ranger VIII* Trajectory Analysis

**Launch phase.** The *Ranger VIII* spacecraft was launched at 17:05:00.795 GMT on February 17, 1965, from the Eastern Test Range at Cape Kennedy, Florida, using an *Atlas D-Agena B* boost vehicle. The inertial launch azimuth was 94.8 deg east of north. After liftoff, the booster rolled to an azimuth of 95.4 deg and performed a programmed pitch maneuver until booster cutoff. During the sustainer and vernier stages, adjustments in vehicle attitude and engine cutoff times were commanded as required by the ground guidance computer to adjust the altitude and velocity at *Atlas* vernier engine cutoff. After *Atlas-Agena* separation, there was a short coast period prior to the first ignition of the *Agena* engine. At a preset value of sensed velocity increase, the *Agena*

engine was cut off. At this time, the *Agena*-spacecraft combination was coasting in a nearly circular parking orbit in a south-easterly direction at an altitude of 187 km and an inertial speed of 7.80 km/sec. After an orbit coast time of 12.83 min, a second ignition of the *Agena* engine occurred. The ignition time was determined by the ground guidance computer and transmitted to the *Agena* during the *Atlas* vernier stage. 87 sec later, the second *Agena* cutoff occurred with the *Agena*-spacecraft combination in a nominal Earth-Moon transfer orbit. The launch-phase ascent trajectory profile is illustrated in Fig. 1; a sequence of events from launch to acquisition of the Earth by the spacecraft is shown in Fig. 2.

**Cruise phase.** Injection (second *Agena* cutoff) occurred at 17:27:37 GMT near the western coast of Africa at a geocentric latitude and longitude of 2.35 and 350.89 deg, respectively. The *Agena*-spacecraft combination was at an altitude of 205 km and traveling at an inertial speed of 10.941 km/sec. At 2 min, 37 sec after injection, the *Agena* separated from the spacecraft, performed a programmed yaw maneuver, and ignited its retrorocket. The retrorocket impulse was designed to eliminate interference with the spacecraft operation and reduce the chance of the *Agena* impacting the Moon. Tracking data indicated that the *Agena* passed the upper trailing edge of the Moon at an altitude of 15,825 km about 6 hr after *Ranger VIII* impact.

The spacecraft, which did not enter the Earth's shadow, acquired the Sun 8 min, 40 sec after the solar panels had been extended. Sun acquisition occurred 12 min, 33 sec after injection. Within 1 hr after injection, the spacecraft was receding from the Earth in almost a radial direction with decreasing speed. This reduced the geocentric angular rate of the spacecraft (in inertial coordinates) until, at 1.5 hr after injection, the angular rate of the Earth's rotation exceeded that of the spacecraft. This caused the Earth's track of the spacecraft (Fig. 3) to reverse its direction from increasing to decreasing Earth longitude. At 20:40:10 GMT, the spacecraft acquired the Earth, thus attaining the designed cruise mode. Plots of the geocentric distance and inertial speed of the probe as well as the Earth-probe-Sun (EPS), Sun-probe-Moon (SPM), and Earth-probe-Moon (EPM) angles as functions of time from launch are presented in Figs. 4 through 6.

Tracking data gathered and analyzed prior to the mid-course maneuver indicated that, without a correction, the spacecraft would miss the Moon on the trailing edge,

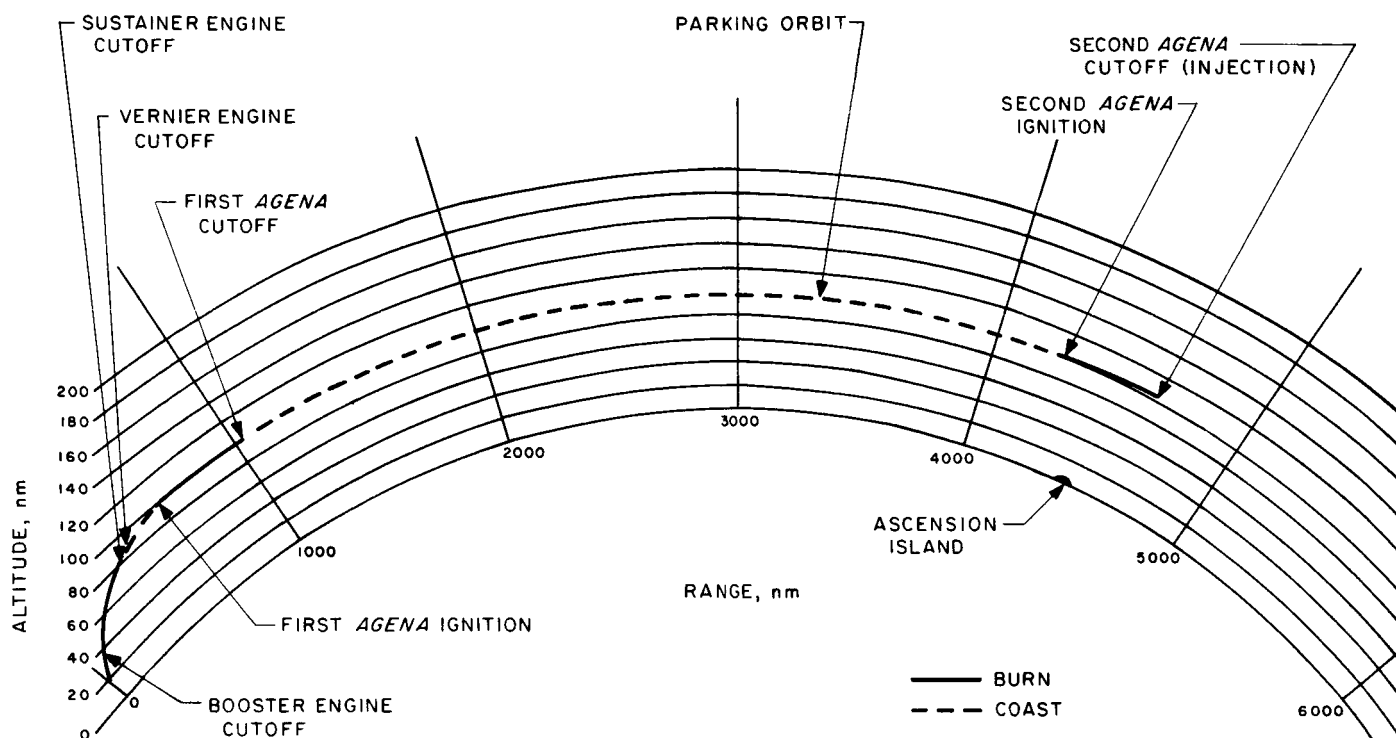


Fig. 1. Ascent trajectory profile

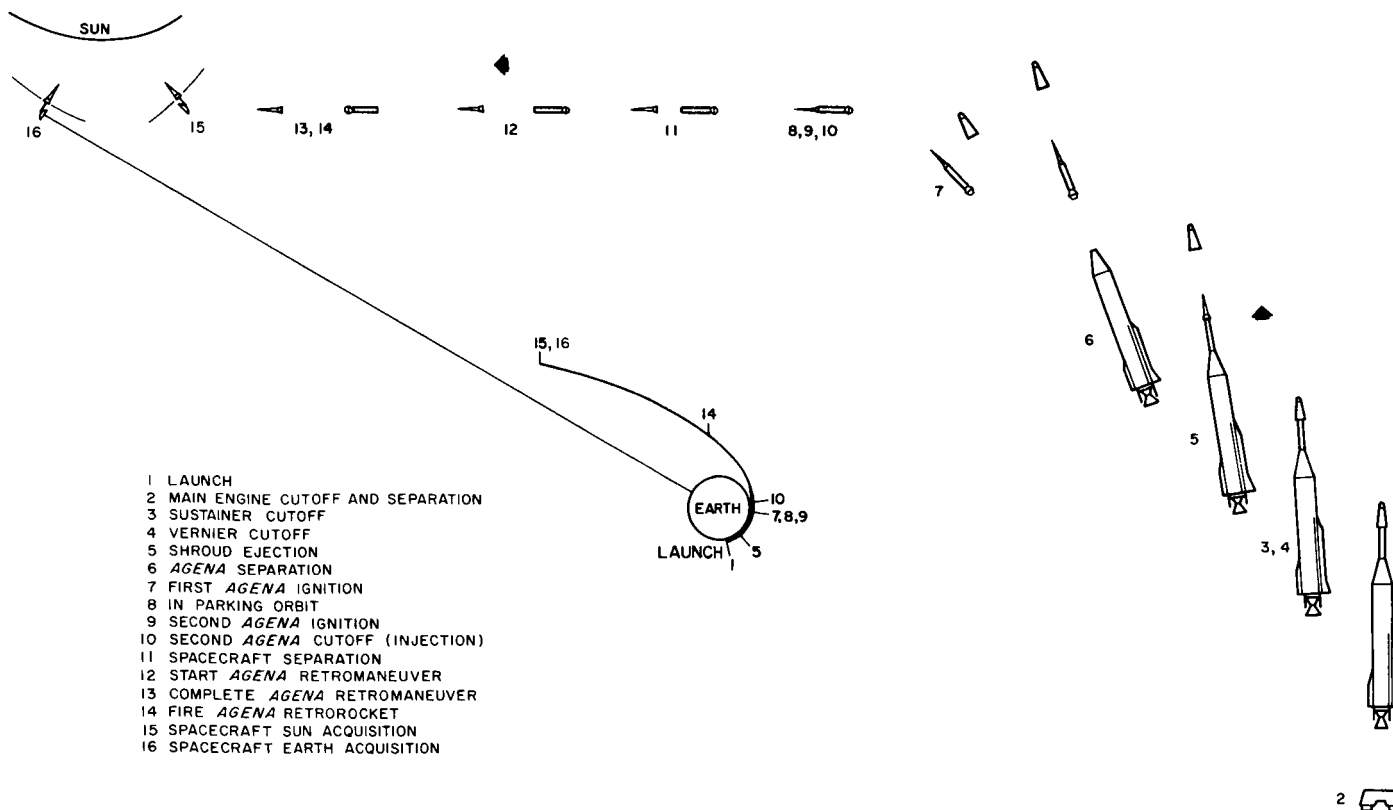


Fig. 2. Sequence of events to Earth acquisition

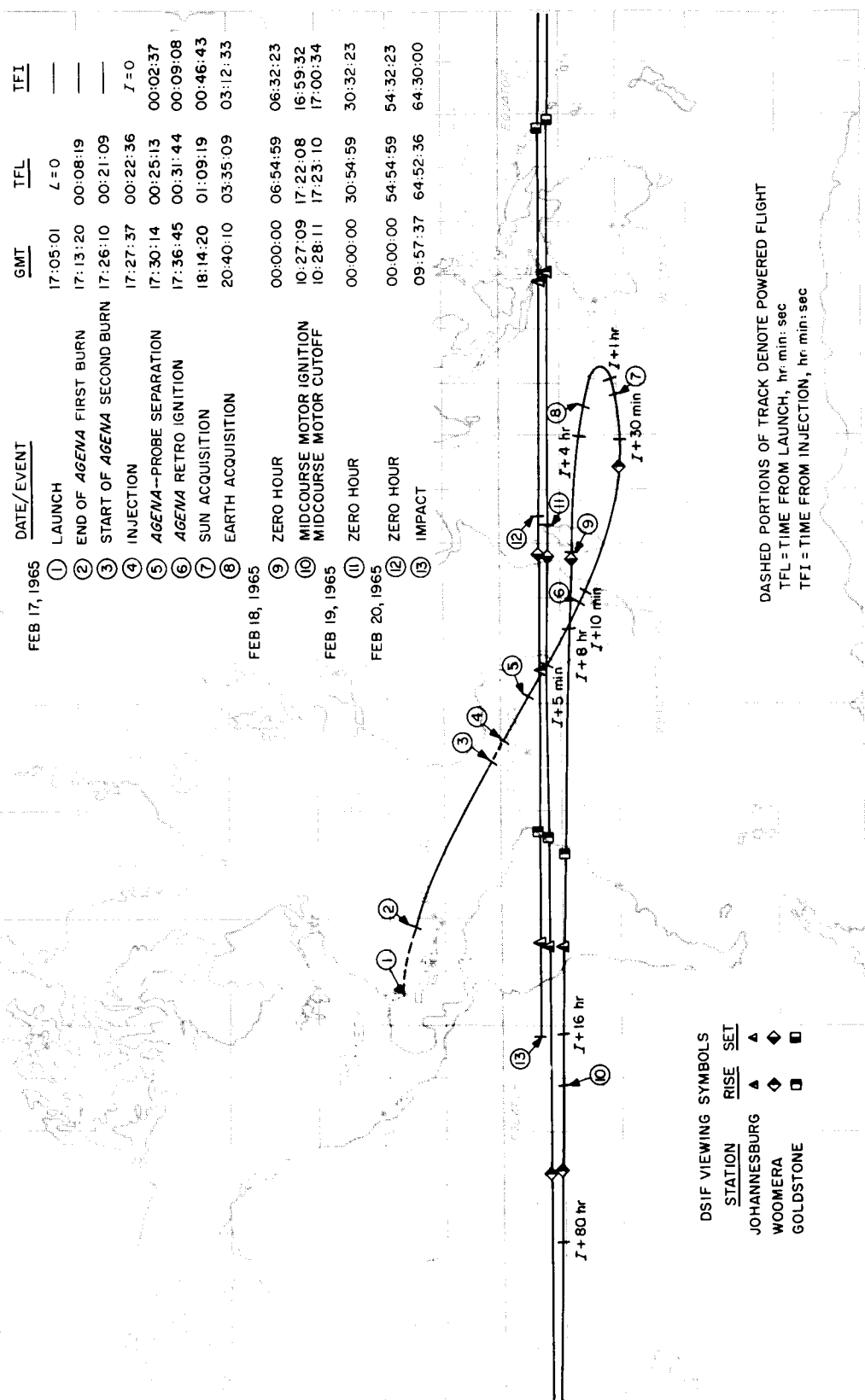


Fig. 3. Earth track of Ranger VIII trajectory

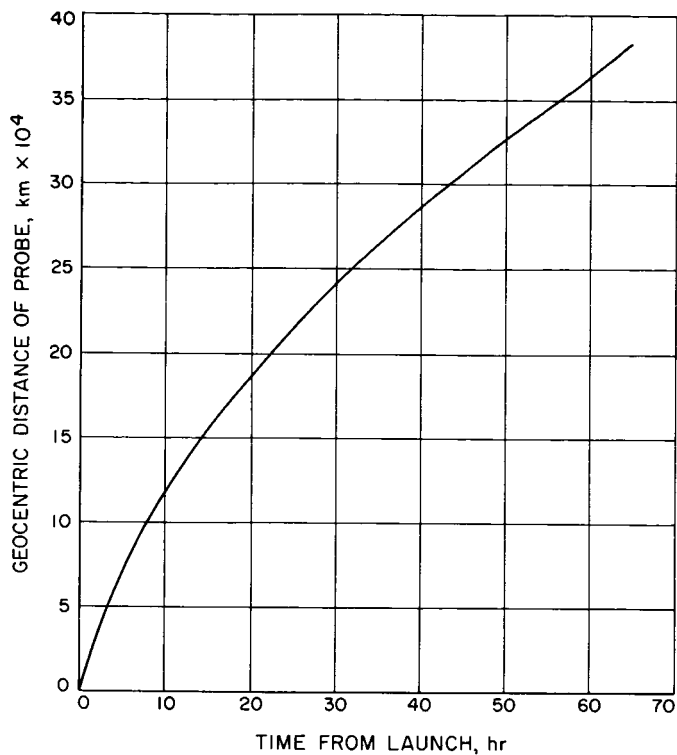


Fig. 4. Geocentric distance of probe vs time from launch

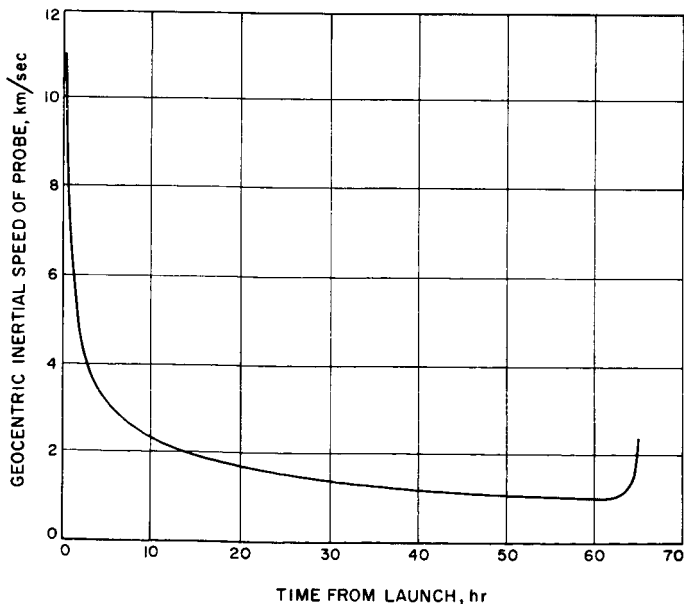


Fig. 5. Geocentric inertial speed of probe vs time from launch

with a closest approach altitude of 1868 km at a selenocentric latitude and longitude of 19 and 75 deg, respectively. The transit time from injection to impact would

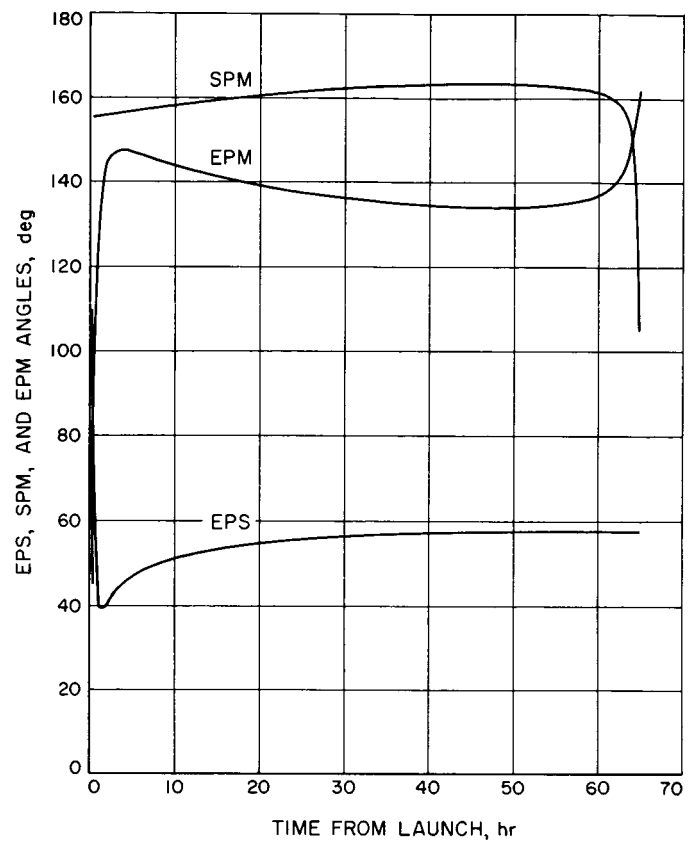


Fig. 6. Earth-probe-Sun (EPS), Sun-probe-Moon (SPM), and Earth-probe-Moon (EPM) angles vs time from launch

have been 66.46 hr. The *Ranger VIII* transfer trajectory is illustrated in Fig. 7.

**Midcourse maneuver phase.** In order to alter the trajectory so as to impact a selected aiming point at a selenocentric latitude of 3 deg and longitude of 24 deg, midcourse maneuver calculations indicated a requirement for a 36.55-m/sec increment of velocity (60.93-m/sec maximum capability). In addition, this correction was selected to adjust the flight time from injection to impact to be 64.494 hr, thus allowing the TV camera backup turn-on clock to be utilized as designed; i.e., with this flight time, the clock would turn on the F-cameras 12 min prior to impact. To properly align the thrust direction of the midcourse motor for the burn, an 11.60-deg roll turn and 151.75-deg pitch turn were required. The midcourse motor was ignited at 10:27:09 GMT on February 18, 1965, at which time the spacecraft was at a geocentric distance of 169,039 km and traveling with an inertial speed of 1.811 km/sec relative to the Earth. At the end of the 52-sec burn of the midcourse motor, the geocentric

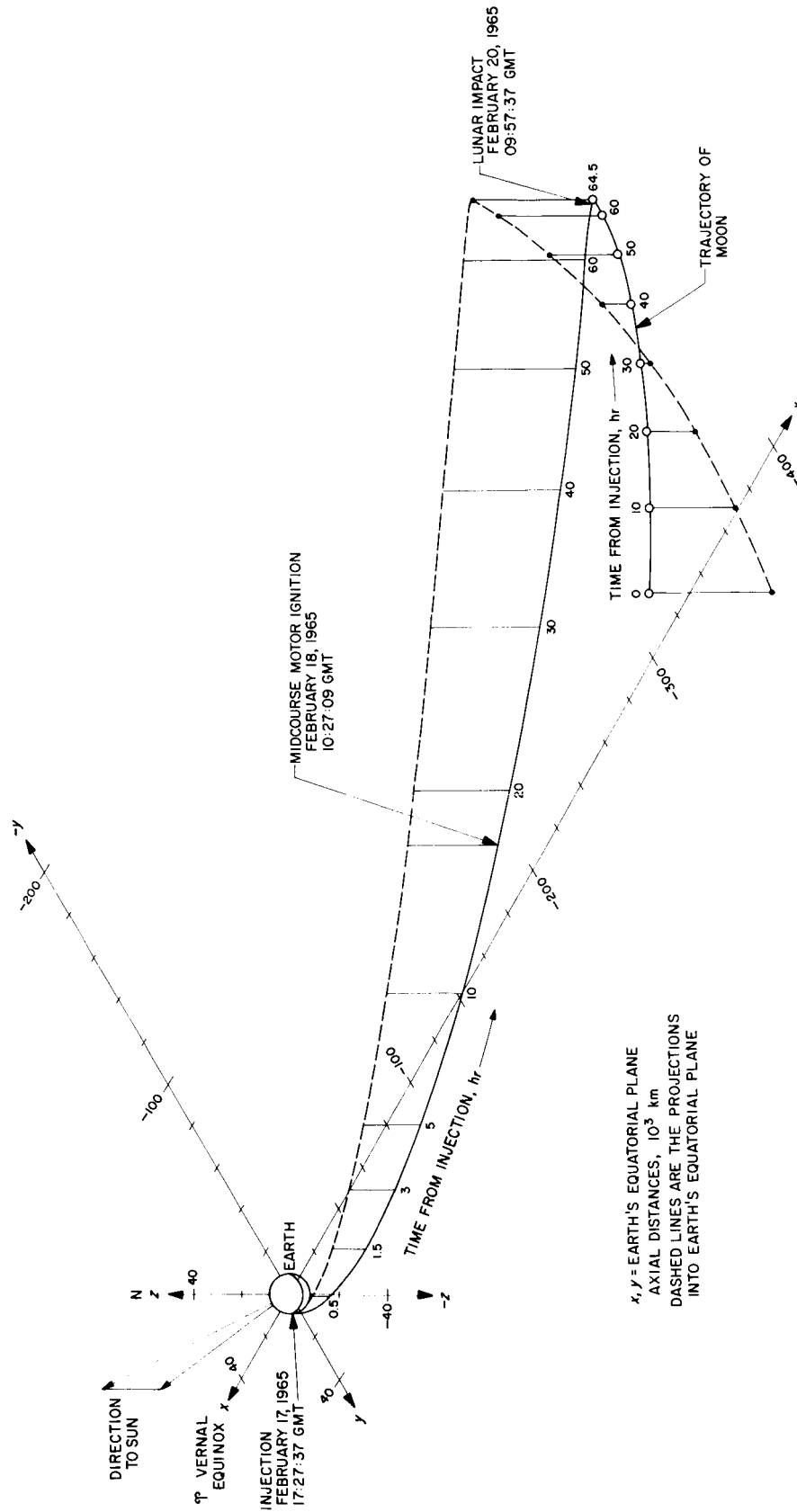


Fig. 7. Ranger VIII transfer trajectory

distance had increased to 169,148 km, and the inertial speed relative to the Earth had increased to 1.840 km/sec. Analog data received at the Goldstone Space Communications Station and relayed to the JPL Space Flight Operations Facility gave positive indication that the midcourse maneuver and motor burn had been executed precisely. This was further verified by the observed doppler data, which were essentially the same as those predicted for the maneuver. Injection and encounter conditions for the premidcourse orbit used to determine the midcourse maneuver are given in Table 1.

**Postmidcourse maneuver cruise phase.** Following the midcourse maneuver, the spacecraft reacquired the Sun and Earth, thus returning to the cruise mode. At about

59 hr from injection and at a geocentric distance of 359,000 km, the spacecraft's inertial speed relative to the Earth reached a minimum value of 1.012 km/sec. At this point, the spacecraft was about 31,800 km from the lunar surface with an inertial speed of 1.31 km/sec

**Table 2. Definition of symbols (with Earth as central body)**

$R$	probe radius distance, km
$\phi$	probe geocentric latitude, deg
$\theta$	probe east longitude, deg
$V$	probe Earth-fixed velocity, km/sec
$\gamma$	path angle of probe Earth-fixed velocity vector with respect to local horizontal, deg
$\sigma$	azimuth angle of probe Earth-fixed velocity vector measured east of true north, deg
$x, y, z$	vernal equinox Cartesian coordinates, in km, in a geocentric equatorial system. The origin is the center of the central body. The principal direction ( $x$ ) is the vernal equinox direction of date, and the principal plane ( $x, y$ ) is the Earth equatorial plane of date. $z$ is along the direction of the Earth's spin axis of date
$\dot{x}, \dot{y}, \dot{z}$	first-time derivatives of $x, y$ , and $z$ , respectively: i.e., Cartesian components of the probe space-fixed velocity vector, km/sec
$a$	semimajor axis, km
$e$	eccentricity
$i$	inclination, deg
$\Omega$	longitude of the ascending node, deg
$\omega$	argument of pericenter, deg
$\nu$	true anomaly, deg

**Table 1. Orbit used for determination of the Ranger VIII midcourse maneuver**

Injection conditions <sup>a</sup>	
Epoch	February 17, 1965; 17:27:37 GMT
Earth-fixed sphericals	
$R$	6583.1948 km
$\phi$	2.3530941 deg
$\theta$	350.89155 deg
$V$	10.523490 km/sec
$\gamma$	1.7277902 deg
$\sigma$	119.97585 deg
Inertial Cartesian	
$x$	5018.6690 km
$y$	4251.8658 km
$z$	270.29093 km
$\dot{x}$	-5.7934230 km/sec
$\dot{y}$	7.6624908 km/sec
$\dot{z}$	-5.2380550 km/sec
Orbital elements	
$a$	288489.38 km
$e$	0.97719987
$i$	28.808329 deg
$\Omega$	224.55678 deg
$\omega$	171.74995 deg
$\nu$	3.3623356 deg
Encounter conditions and miss parameters	
Closest approach epoch	February 20, 1965; 11:54:38.397 GMT
Selenocentric altitude	1867.9459 km
Selenocentric latitude	19.326950 deg
Selenocentric longitude	74.723510 deg
Time of flight from injection	66.456 hr <sup>b</sup>
$ B $	6335.8717 km <sup>c</sup>
$B \cdot T^d$	6137.6450 km
$B \cdot R^d$	-1572.4450 km
<sup>a</sup> See Table 2 for definition of symbols. <sup>b</sup> 1 $\sigma$ uncertainty of 5.1 sec. <sup>c</sup> 1 $\sigma$ uncertainty of 12.3 km. <sup>d</sup> $B \cdot T$ and $B \cdot R$ are referenced to the true lunar equator (Fig. 8). (For Ranger VIII work, the true lunar equator is used as the reference plane. If $N$ is a unit vector in the lunar north direction, then $T = S_I \times N$ and $R = S_I \times T$ .)	

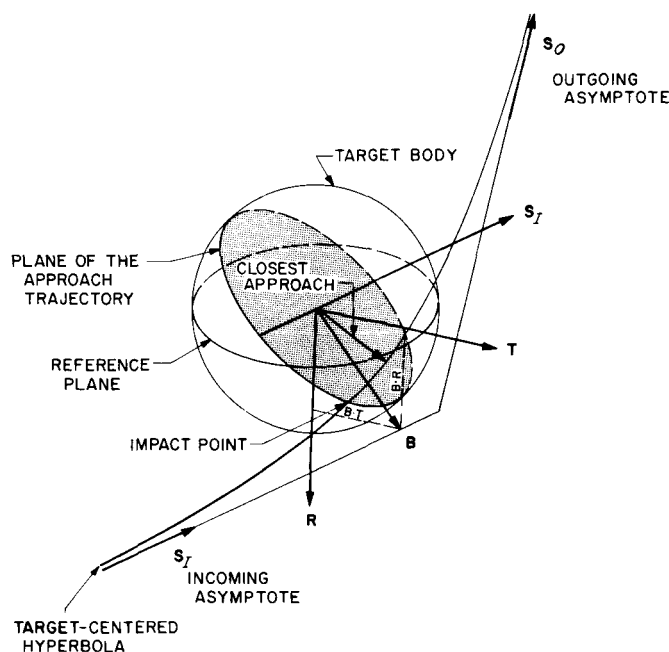


**Fig. 8. Definition of the miss parameter B**

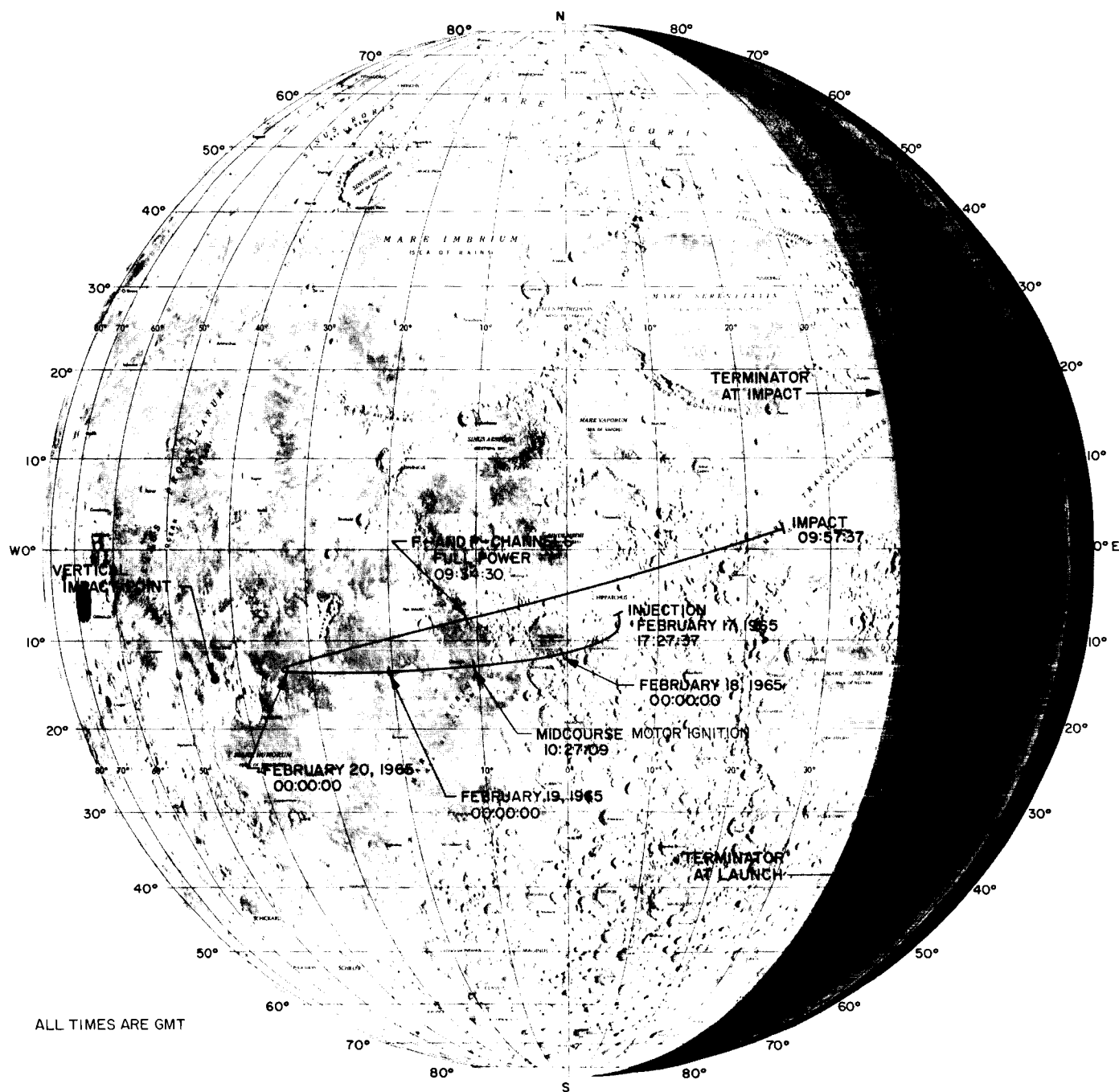


Fig. 9. Lunar track of *Ranger VIII* trajectory



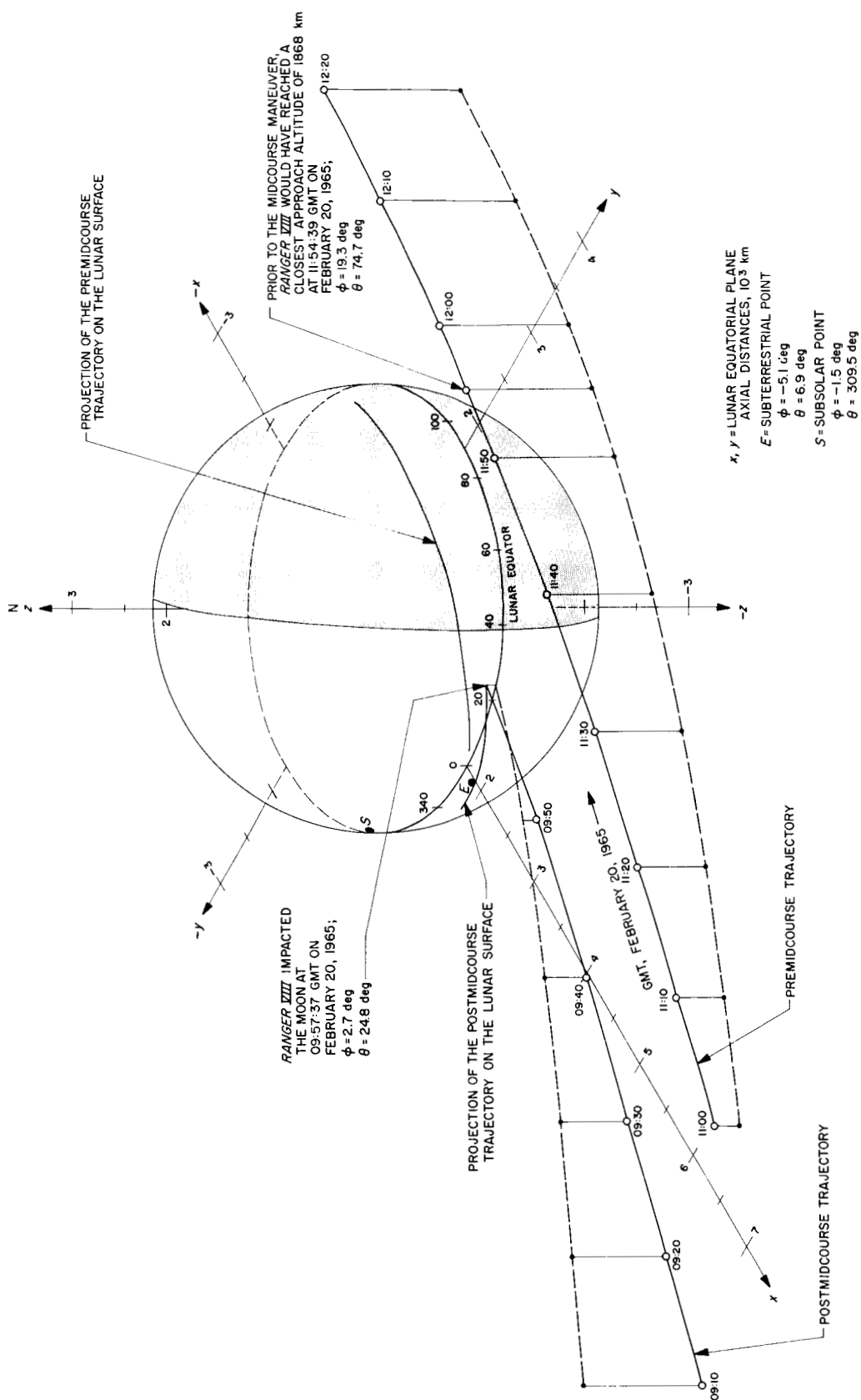


Fig. 10. Ranger VIII premidcourse and postmidcourse encounter trajectories

relative to the Moon. Due to the lunar gravitational field, the spacecraft's velocity then began to increase.

Postmidcourse tracking data were analyzed and resolved the lunar encounter conditions to a high degree of accuracy. Lunar impact was indicated to occur at a selenocentric latitude and longitude of 2.71 and 24.81 deg, respectively, with a flight time from injection of 64.50 hr. The encounter conditions and the corresponding postmidcourse initial conditions are presented in Table 3.

**Encounter phase.** During the encounter phase of the *Ranger VIII* flight, the spacecraft raced toward lunar impact with increasing acceleration due to the pull of the lunar gravitational field. At 1 hr before impact, at a lunar altitude of 6154 km, the speed of the probe relative to the Moon had increased to 1.621 km/sec. No

terminal maneuver to realign the TV cameras' pointing direction was necessary.

At 09:34:30 GMT on February 20, 1965, while at an altitude of 2511 km above the lunar surface, full power on Channels F and P was verified. Minutes later, at 09:57:35.966 GMT, *Ranger VIII* crashed onto the lunar Sea of Tranquility at an impact speed of 2.651 km/sec and at a path angle of  $-41.7$  deg. The spacecraft had encountered the Moon in a direct motion along a hyperbolic trajectory, the incoming asymptote direction being at an angle of  $-13.59$  deg to the lunar equator and with the orbit plane inclined 16.06 deg to the lunar equator.

The trace of the trajectory on the lunar surface from injection to impact is given in Fig. 9; the traces of the lunar approach portions of the premidcourse and postmidcourse orbits are illustrated in Fig. 10. Figs. 11 through 15 present trajectory parameters plotted versus GMT prior to impact of the *Ranger VIII* spacecraft on the Moon.

Table 3. First postflight orbit of *Ranger VIII*

Postmidcourse conditions <sup>a</sup>	
Epoch	February 18, 1965; 10:28:08 GMT
Earth-fixed sphericals	
$R$	169142.90 km
$\phi$	$-12.683817$ deg
$\theta$	$255.09762$ deg
$V$	$11.803385$ km/sec
$\gamma$	$8.7308957$ deg
$\sigma$	$270.97074$ deg
Inertial Cartesian	
$x$	$-154760.64$ km
$y$	$-57264.116$ km
$z$	$-37138.819$ km
$\dot{x}$	$-1.5522736$ km/sec
$\dot{y}$	$-0.96692909$ km/sec
$\dot{z}$	$-0.20057075$ km/sec
Orbital elements	
$a$	$300051.42$ km
$e$	$0.97889288$
$i$	$30.732920$ deg
$\Omega$	$222.54946$ deg
$\omega$	$173.49243$ deg
$\nu$	$161.06173$ deg
Impact parameters	
Impact epoch	February 20, 1965; 09:57:37.18 GMT
Selenocentric latitude	$2.7129144$ deg
Selenocentric longitude	$24.806900$ deg
Time of flight from injection	$64.500$ hr <sup>b</sup>
$ B $	$2909.4591$ km <sup>c</sup>
$B \cdot T^d$	$2876.3865$ km
$B \cdot R^d$	$-437.43943$ km
<sup>a</sup> See Table 2 for definition of symbols. <sup>b</sup> 1 $\sigma$ uncertainty of 0.1 sec. <sup>c</sup> 1 $\sigma$ uncertainty of 8.6 km. <sup>d</sup> $B \cdot T$ and $B \cdot R$ are referenced to the true lunar equator (Fig. 8). (For <i>Ranger VIII</i> work, the true lunar equator is used as the reference plane. If $N$ is a unit vector in the lunar north direction, then $T = S_I \times N$ and $R = S_I \times T$ .)	

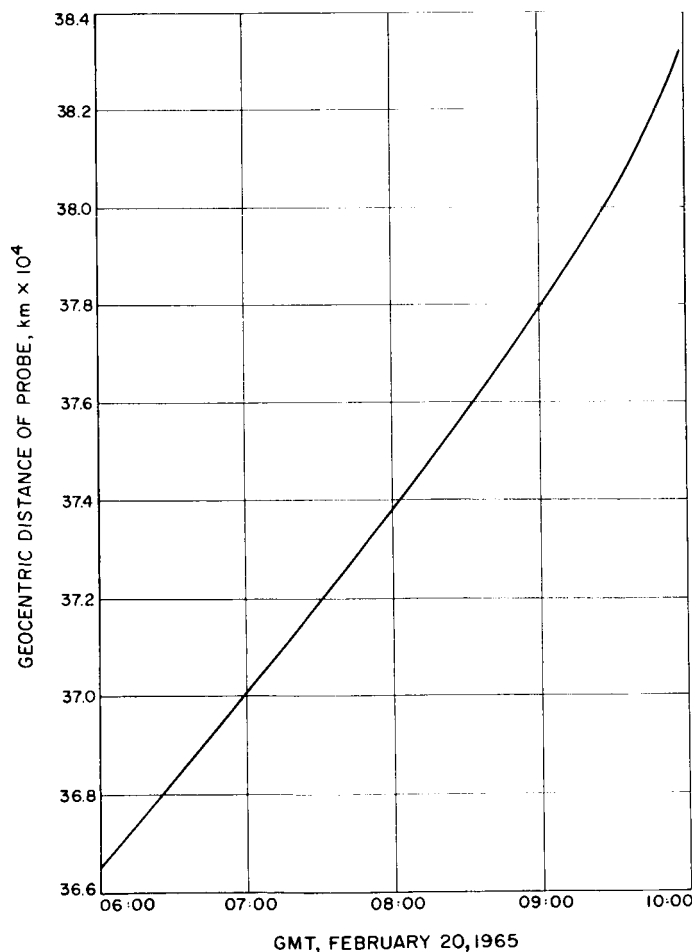
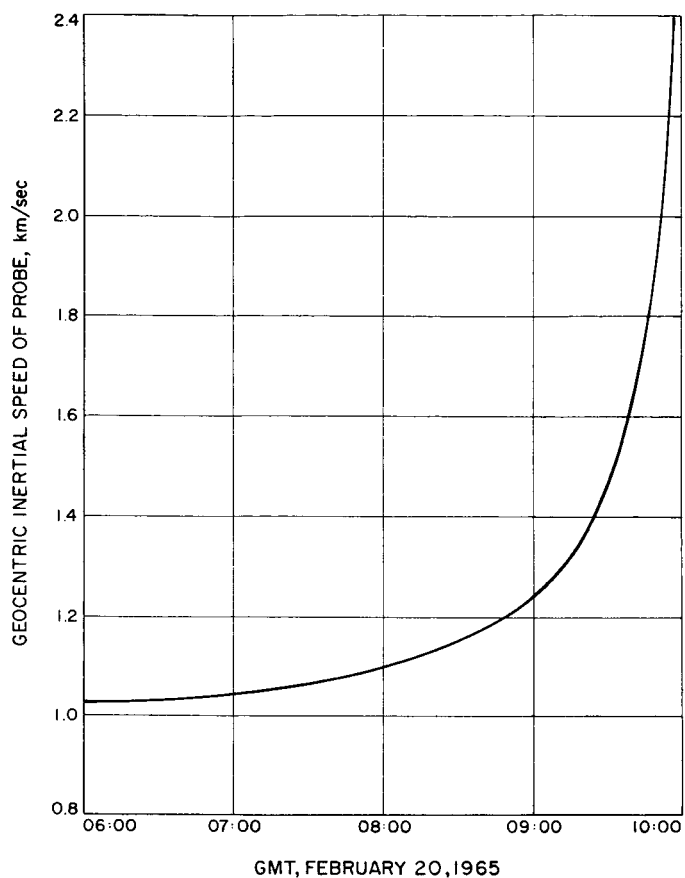
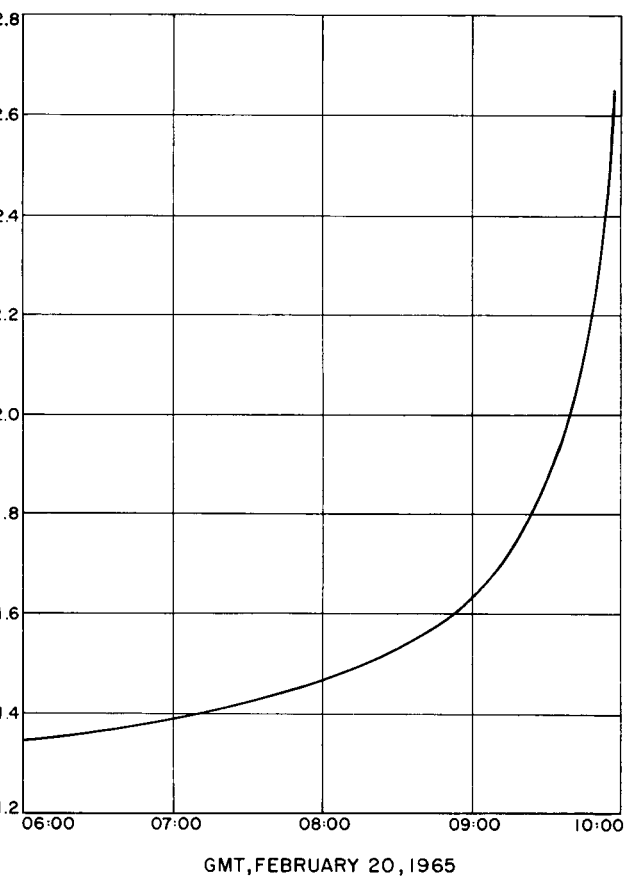
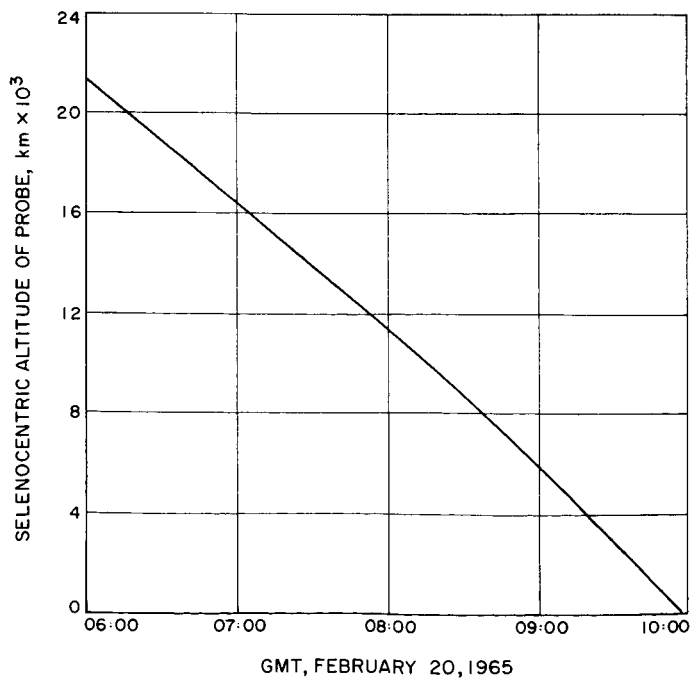


Fig. 11. Geocentric distance of probe vs GMT at lunar encounter



**Fig. 12. Geocentric inertial speed of probe vs GMT at lunar encounter**



**Fig. 14. Selenocentric inertial speed of probe vs GMT at lunar encounter**

**Fig. 13. Selenocentric altitude of probe vs GMT at lunar encounter**

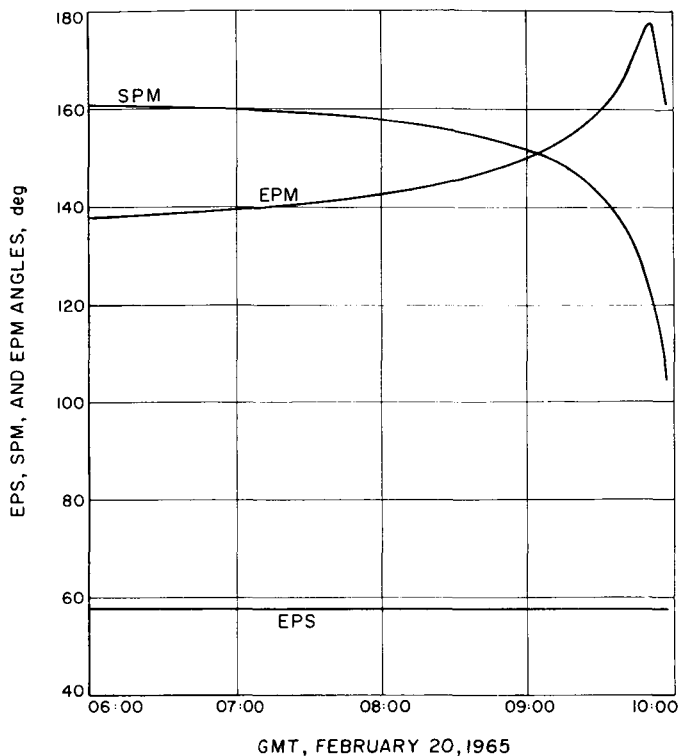


Fig. 15. Earth-probe-Sun (EPS), Sun-probe-Moon (SPM), and Earth-probe-Moon (EPM) angles vs GMT at lunar encounter

## C. Mark II L-Band Communication System Performance During the Block III Missions

The Mark II L-band communication system was described in SPS 37-22, Vol. VI, pp. 2-5. This system

(Fig. 16) was flown on the *Ranger* Block III missions. Its performance on *Rangers* VI and VII was as predicted; however, on *Ranger* VIII, the following anomaly occurred: 3 sec after the spacecraft Channel B-12 event blip indicated the end of the midcourse roll turn, the output of the spacecraft L-band transmitter dropped. The drop in power varied between 23 and 41 db below normal until the midcourse motor burn (a period of approximately 25 min), when the power returned to normal. The communication system operated without further anomalies during the remainder of the mission. The drop in power was sufficient to put the ground-received signal below the telemetry threshold for much of this period. The signal strength varied enough, however, that some telemetry data were recovered. The ground-received carrier power was above threshold for most of the period, and all indications are that the Deep Space Instrumentation Facility/spacecraft system remained in two-way lock throughout most of this period.

An analysis of the recovered data led to the conclusion that a likely cause of the failure was a conductive particle, floating in the zero-*g* environment, that was moved so as to cause a short circuit by the cessation of the roll turn and was dislodged by the motor burn. Concurrent empirical tests on a representative radio system showed that the occurrence of such a short in either the transponder transmitter multiplier chain or the input probe of the 3-w amplifier (internal to the cavity) could have produced the anomaly. It was concluded that, since this was not a systematic failure and since chances of its repetition were remote, it would be safe to fly the scheduled *Ranger* IX mission using the L-band communication system without further investigation and subsequent delay. The *Ranger* IX communication system performed as predicted throughout the mission, and no anomalies occurred.

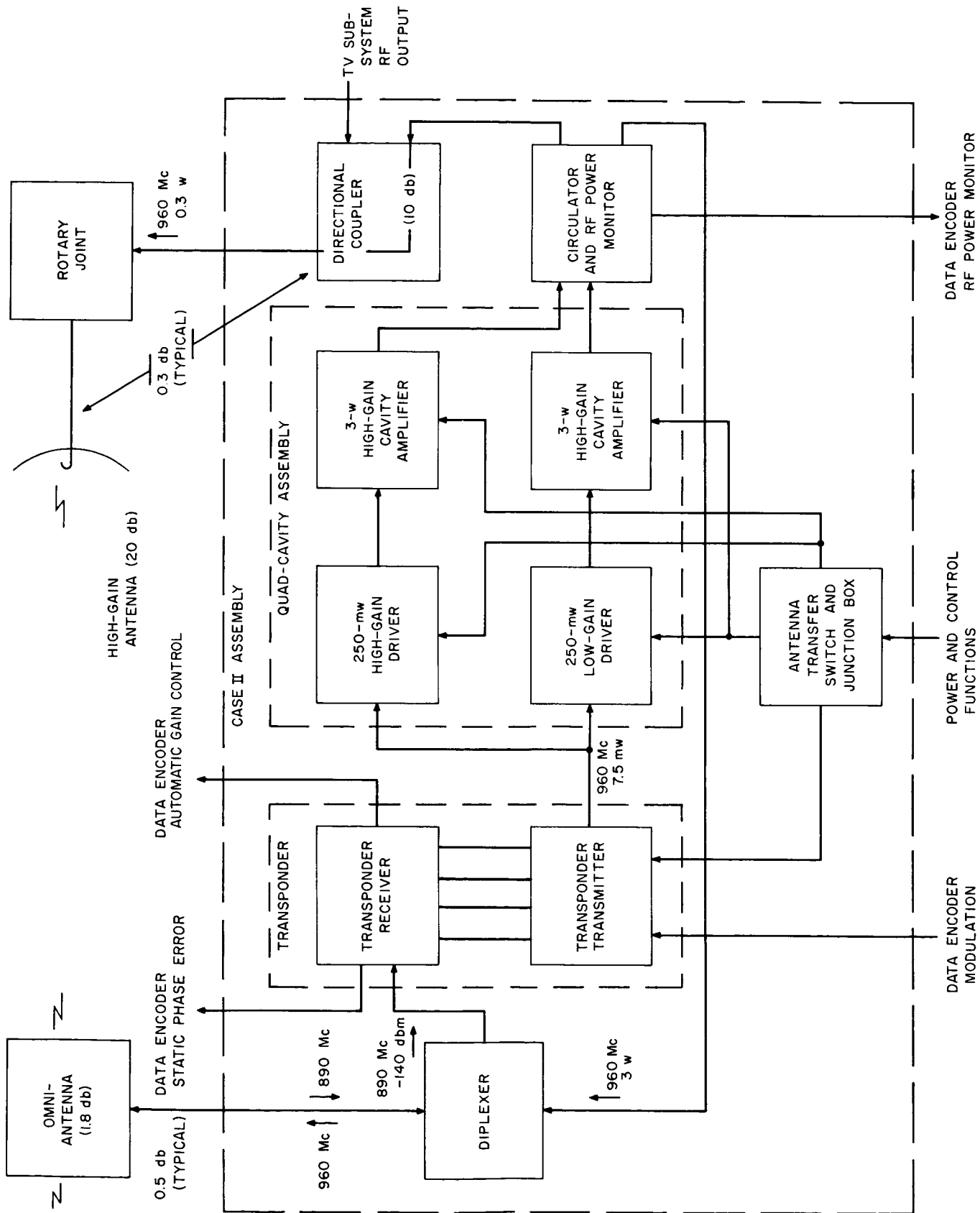


Fig. 16. Mark II L-band communication system

## II. *Surveyor* Project

### A. Introduction

Calculated to span the gap between the *Ranger* flights and Project *Apollo*, the *Surveyor* spacecraft is designed to take the next step in lunar technology by attempting soft landings on the Moon. The first launches will be engineering test missions to demonstrate system capability up to soft landing and limited postlanding operations. The engineering payload includes elements of redundancy, diagnostic telemetry, touchdown instrumentation, and survey TV.

Following the engineering test missions, the objectives are to extend our knowledge of lunar conditions and to verify the suitability of *Apollo* landing sites. The science payload is planned to consist of two-camera TV, and micrometeorite ejecta, single-axis seismometer, alpha particle scattering, soil sampler, and touchdown dynamics experiments.

Hughes Aircraft Company (HAC), Space Systems Division, is under contract to develop and fabricate the first seven spacecraft. The JPL Space Flight Operations Facility and Deep Space Network (Mission Operations System) will be utilized for flight control and tracking. The first flight, using an *Atlas-Centaur* launch vehicle, is scheduled for late-1965.

### B. Systems Testing

#### 1. SC-1 Flight Spacecraft

Two electromagnetic interference tests were performed at HAC on the SC-1 flight spacecraft during this reporting period. The first was a mission sequence through injection similar to previous tests, but with the upgraded units installed and with "live" pyrotechnics. The other test was a special test for RF spectrum measurement to determine the interference effects at the spacecraft operating frequency. Data indicated that RF noise propagated from the altitude marking radar, the radar altimeter and doppler velocity sensor, and the spacecraft transmitters was well within the prescribed limits. Following these tests, flight-acceptance vibration tests of the SC-1 spacecraft were conducted.

#### 2. T-21 Prototype System-Test Spacecraft

The T-21 type-approval vibration tests begun at HAC during the last reporting period have been completed. Transponder and transmitter phase jitter, transmitter frequency stability, and commutator data were monitored to evaluate system performance in the vibration environment. Even at the type-approval high-energy vibration levels, phase lock was maintained, commutated data

processing was unaffected, and transmitter frequency remained within specification limits.

The final checkout of the T-21 spacecraft prior to shipment to General Dynamics/Convair at San Diego for the combined systems test with the *Atlas-Centaur 7* launch vehicle used three of the actual procedures to be employed during that test and those at the Eastern Test Range (ETR): (1) a sequence of tests to verify proper operation of the RF and power subsystems, (2) the system readiness test performed by RF space link to the *Surveyor* vehicle after shroud encapsulation, and (3) a verification of the squib circuits and a more extensive test of the TV than was done in (2). Any discrepancies which occurred were noted in the data package which accompanied the T-21 to San Diego. These data will be correlated with the data taken there and later with the data taken at the ETR.

The T-21 spacecraft is shown in its arrival configuration at the NASA Combined Systems Test Facility at General Dynamics/Convair in Fig. 1. The combined systems testing was performed in three phases: the system readiness test, the final countdown test, and the simulated flight test. Following the tests, a combined acceptance-test data review was conducted, and discrepancies were satisfactorily resolved at that time. The spacecraft was then

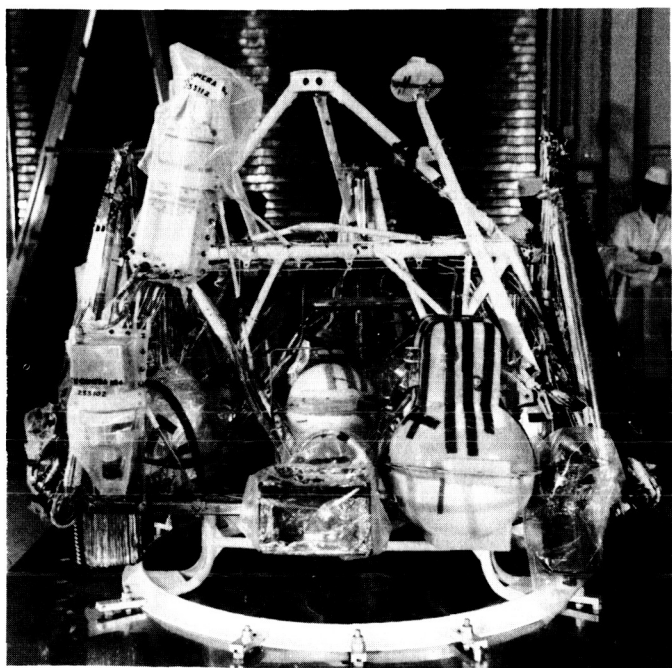


Fig. 1. T-21 spacecraft in arrival configuration at General Dynamics/Convair

demated from the *Centaur* vehicle, decapsulated, disassembled, packaged for shipment, and shipped to the ETR on May 29, 1965, as scheduled.

Following the receipt, inspection, and assembly of the T-21 spacecraft at the ETR, the initial spacecraft checkout tests were conducted. The T-21 spacecraft will be used to check the ETR facilities for processing an engineering-model flight spacecraft and to preview problems that may exist during the launch operations of a flight spacecraft.

### 3. SD-2 Spacecraft Dynamic Model

The *Surveyor* dynamic model SD-2 with its *Atlas-Centaur 6* launch vehicle successfully completed the interim combined systems test at General Dynamics/Convair and was shipped to the ETR and prepared for prelaunch operations. The dynamic model system test equipment assembly was reactivated, and the transponder was tested and calibrated.

### 4. GT-1 Group Test Vehicle

The basic frame of GT-1 was received for system testing and installed on System Test Equipment Assembly (STE) 1 at HAC. Group tests were performed on the boost regulator, battery charge regulator, and central command decoder spare units. Following a 2-wk period for additional substructure mounting, the vehicle was installed on STEA 4. Four sets of spacecraft units will be group-tested with the GT-1 vehicle on STEA 4: SC-1, SC-3, SC-2 units not group-tested prior to upgrade, and SC-2 units requiring retest after extensive upgrade.

### 5. T-2N-1 Descent Dynamics Test Vehicle

Closed-loop tests to prove the compatibility of operation of the T-2N-1 vehicle and the operations console were successfully completed at HAC. The final portion of functional testing is under way, and no major functional problems have been encountered thus far.

### 6. T-2N-R Recovery System Test Vehicle

The functional-test cargo-fit check and the vehicle/cargo-support vibration tests of the T-2N-R vehicle were completed at HAC. One landing shock test was performed, and the data revealed an excessive amount of landing shock. Trapezoidal air bags of a new design proved satisfactory in additional tests, and a relief valve was successfully tested for maintaining uniform bag pres-

sure as a function of time following inflation. Air-bag drop testing was conducted, and the T-2N-R vehicle was then shipped to the Air Force Missile Development Center.

## C. Flight Control

### 1. Closed-Loop System Test Criteria

To provide increased assurance that the flight control system is performing properly, closed-loop criteria, in the form of gain and phase margins at specified frequencies, have been developed for use during the solar-thermal-vacuum and following test phases of the SC-1 flight spacecraft. Suitability of the criteria and validity of the system test equipment assembly (STEA) simulation were evaluated by conducting identical tests with both STEA and analog computer laboratory equipment, utilizing the same flight control electronics unit in each case. Consistent results were obtained from the two tests.

### 2. Canopus Sensor Performance

Tests were conducted to determine the effect on Canopus sensor performance of reflected light from the lunar surface as the spacecraft approaches the Moon before the pre-retrorocket maneuver. Several Canopus sensor shade configurations were tested simulating the range of all possible lunar approach angles. Test results indicated that an extended shade with light baffles will permit proper sensor performance without degradation due to reflected moonlight.

A concurrent test program to determine the effect on sensor performance of reflected sunlight from nearby spacecraft structures was also completed. Several sensor shade configurations were tested, and test results again indicated proper sensor performance with the new baffled shade. These shades are now being fabricated for installation at the ETR during the flight-control sensor-group checkout.

The most sensitive component of the *Surveyor* vehicle system to nuclear radiation appears to be the photomultiplier detector in the Canopus unit. Sizable currents have been generated by nuclear radiation with charged particle and X-ray flux rates which are considerably smaller than

those that will be experienced on the *Surveyor* mission, particularly in the Van Allen belt region. This caused concern about satisfactory operation of the Canopus sensor in detecting the Canopus light signal while in the intense part of the radiation environment. Recent experimental test measurements point toward satisfactory operation of the Canopus sensor, even in beta-particle radiation fluxes exceeding the maximum severity expected in the Van Allen belt.

### 3. Acquisition Sun Sensor Performance

Studies were conducted to determine the effect of reflections from the *Centaur* stage on acquisition Sun sensor performance. On the SC-1 flight spacecraft, the *acquire Sun* command will be generated approximately 10 min after separation by a signal from the solar-panel lock switch. The *Centaur-Surveyor* distance at that time will be great enough that the probability of false triggering will be extremely low. For later spacecraft with the fully automatic 51-sec-delay system, however, the *Centaur* stage can be as close as 35 ft to the *Surveyor* spacecraft. Assuming the *Centaur* stage to be a 52% reflecting cylinder, the reflected sunlight input from the stage is below the threshold of the sensor, although there is still the possibility that reflections from small flat surfaces might trigger the sensor. Further studies are being conducted to determine the necessity and feasibility of increasing the 51-sec delay.

### 4. Roll Actuator Design

During the last vibration sweep in type-approval testing, the roll actuator apparently moved with respect to its mounting bracket, thereby causing the alignment pin on the roll actuator shaft to fracture. To correct this problem, the friction coefficients of mounting surfaces and torque levels of attachment fasteners have been increased, and locknuts and studs instead of lock-wired screws will be used for attachment. Also, a recent thermal investigation of the radiant heating flux of the vernier engine resulted in the incorporation of a thermal shield on the roll actuator to protect the pinpuller wiring harness and its connector as well as a portion of the roll actuator itself. The improved mounting and the thermal shield are shown in Fig. 2.

Vacuum firing tests of a single vernier engine attached to a flight-type mounting bracket and an operating flight-type roll actuator were conducted at the JPL Edwards Test Station. To obtain thermal-vacuum data, a nominal mission profile of vernier engine thrust was run, allowing



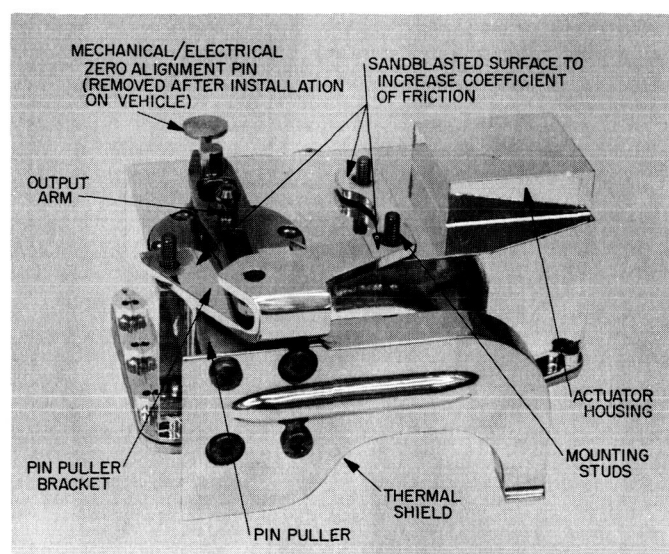


**Fig. 2. Roll actuator, showing improved mounting and thermal shield**

time for temperatures to return to ambient between mid-course and terminal descent firings. Preliminary data analysis indicates that test results were in good agreement with predicted values.

Further firing tests were made at near-maximum thrust while roll actuator responses to various inputs were measured. The reduced data will be compared with analytical studies and response measurements obtained under laboratory conditions. During the last firing test at near-maximum thrust, a mechanical failure occurred in the thermal isolator assembly that mounts the roll-actuator vernier-engine bracket to the spaceframe. A modification of the thermal isolator assembly is in progress, and an additional vacuum firing is planned to verify the modified design.

## D. Electronics

### 1. Altitude Marking Radar

Early tests on two altitude marking radar systems indicated that the detection threshold drifted well beyond the allowable limits and was extremely sensitive to line-voltage and temperature variations. Investigation revealed that most of the threshold drift was caused by: (1) noise

generated in the transmitter-receiver tube, and (2) excessive noise in the local oscillator. In both cases, the noise was modulated with a ripple that was synchronous with the range gates, which resulted in a shift in the integrated range gate output.

To eliminate this problem, the following action was taken: The ripple voltage on the local oscillator power supply was reduced, the alignment procedure for the local oscillator was improved to reduce the excess noise, and the transmitter-receiver tubes were eliminated. A regulator was added to reduce the ripple on the local oscillator input voltage, and subassembly test requirements were prepared to ensure that only those units with acceptable noise figures are used on the radar.

The two systems were tested after incorporation of these improvements. Threshold drift was no longer a problem, and a significant improvement in receiver sensitivity was realized.

### 2. Battery Charge Regulator

During system testing of the T-21 prototype spacecraft, it was found that the charging function of the battery charge regulator became erratic when the 29-v regulated bus was loaded to more than 50% of full load. Further investigation disclosed that noise pulses appeared on the unregulated bus as the regulated bus load was increased. Noise pulses on the order of 5 v peak-to-peak were observed when the regulated bus was fully loaded.

Laboratory tests established that the optimum charge regulator would not lock up about the solar-panel maximum power point when noise signals were injected into the battery charge regulator output. It was determined that the noise signals injected into the optimum charge regulator feedback loop were causing a false indication of the rate of current change and were thus disrupting normal operation.

An inductive-capacitive filter was inserted into the optimum charge regulator output leads, and noise voltages and frequencies were imposed on the battery charge regulator output. The filter effectively isolated the optimum charge regulator feedback circuits from the noise source, and normal operation of the battery charge regulator charging function was observed throughout the test. The filter was installed in the battery charge regulator unit, which was then returned to the SC-1 flight spacecraft for further testing in the system configuration.

## E. Testing Facilities and Equipment

### 1. Ionization Pressure-Sensing System

A new ionization pressure-sensing system for use during solar-thermal-vacuum tests of the SC-1 flight spacecraft has been designed and fabricated. This system will monitor the evacuated thermal-vacuum chamber pressure. A pressure rise to a predetermined value will cause all system test equipment assembly and spacecraft power to be removed to prevent arcing in the spacecraft.

### 2. Power Monitoring System

The power monitoring technique has been changed considerably during this reporting period. The original power profile monitor unit digitized and commutated up to 30 signals. The commutated signal was then recorded on one channel of the 14-channel system tape recorder. In the new system (Fig. 3), the power profile monitoring unit has been deleted. The shunt signals now go to the JPL 1218 computer and the JPL monitoring printer for recording. The signals also go to the power monitoring

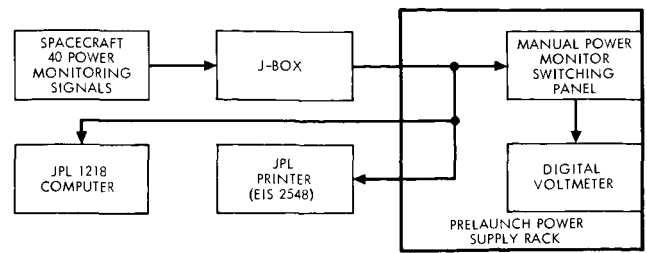


**Fig. 3. New power monitoring system (40 signals)**

switching panel, where they can be manually switched to a digital voltmeter or oscilloscope.

### 3. Data Acquisition Center

A command translator unit was added to the JPL computer data system. The unit receives the FM output of the command generator, demodulates the signal, checks for valid commands, and presents the command in parallel binary-coded-decimal form at the interface to the computer.

# PLANETARY — INTERPLANETARY PROGRAM

## III. *Mariner* Project

### A. Introduction

The early objective of the Planetary-Interplanetary Program is the initial probing of the planets Mars and Venus by unmanned spacecraft. The initial probing of Venus was successfully accomplished by *Mariner II*. The next step toward this objective is the initial probing of Mars by the *Mariner IV* spacecraft, which is now in transit.

The primary objective of the *Mariner C* missions (*Mariner Mars 1964 Project*) is to conduct closeup (flyby) scientific observations of the planet Mars during the 1964-1965 opportunity and to transmit the results of these observations back to Earth. The planetary observations should, to the greatest practical extent, provide maximum information about Mars. TV and cosmic dust experiments and a reasonable complement of field- and particle-measuring experiments are being carried by *Mariner IV*. In addition, an Earth occultation experiment will provide data relating to the scale height and pressure in the atmosphere of Mars.

A secondary objective is to provide experience and knowledge about the performance of the basic engineering equipment of an attitude-stabilized flyby spacecraft during flight in space farther away from the Sun than the Earth. An additional objective is to perform certain field and/or particle measurements in interplanetary space during the trip and in the vicinity of Mars.

The *Mariner III* spacecraft was launched from the Eastern Test Range on November 5, 1964. The nose cone failed to eject from the spacecraft, thereby precluding solar-panel deployment; the battery power was depleted 8 hr, 43 min after launch.

The *Mariner IV* spacecraft was successfully injected into a Mars encounter orbit about the Sun on November 28, 1964. No significant changes in subsystem performance have occurred during this reporting period. Cosmic dust activity appeared to rise in early-May (3 to 4 hits/day), but has since decreased to an average rate of 1 to 2 hits/day. A major milestone was reached

on May 4, 1965, when *Mariner IV* passed the 132-million-mile range from the Sun where radio contact with the Russian *Mars I* probe ended in March 1963. As *Mariner IV* traveled past this point, it was sending back measurements from a region farther away from the Sun and Earth orbit than had been reached by any previous space mission.

All life testing of the *Mariner IV* subsystems will be terminated July 31, proof-test-model testing in support of the flight spacecraft will be stopped by September 1, and the proof test model and its operational support equipment will be placed in storage with the flight spare by October 1.

## B. *Mariner IV* Space Flight Operations

The following standard (planned) events were executed:

- (1) Central computer and sequencer commands MT-3 and MT-4 to update the Canopus cone angle were issued at 14:27:17 GMT on May 7 and 15:53:57 GMT on June 14, respectively. These were the last of the internal commands generated by the central computer and sequencer until the *encounter sequence start* command MT-7.
- (2) The aluminum-silicone absorptivity standard temperature channel ceased operating at 05:43:15 GMT on May 11.
- (3) The central computer and sequencer cyclic pulses were observed on schedule, one every 66⅔ hr.

The nonstandard events which occurred during this reporting period were as follows:

- (1) The spacecraft battery voltage continued to rise. A one-data-number increase was observed on six different days, and, at the end of the reporting period, the voltage was approximately 36.8 v. The cause of this anomaly appears to be either: (a) a small trickle charge fed to the battery through a telemetric transducer, or (b) a leakage of electrolyte in one or more cells. The overcharge condition is not considered serious unless the spacecraft is required to go into a load-sharing mode (required

if the power demands exceed the solar-panel capabilities). All possible efforts were made during encounter planning to ensure that such a mode will not be required.

- (2) Solar flares were detected by the spacecraft radiation and magnetic-field instruments at 23:00 GMT on May 25 and at 19:30 GMT on June 6.
- (3) Disturbances in the roll channel of the attitude-control subsystem were observed on four different days after a long period (47 days) of no detectable perturbations. No loss of Canopus lock was experienced during any of the disturbances.
- (4) The polished-aluminum absorptivity standard temperature channel ceased operating at 15:44:41 GMT on May 17 earlier than expected.

The solar plasma instrument data became unintelligible due to the normal lowering of internal temperatures which results in an increase of the voltage stepping recovery time constant. This condition resulted from a failure in this instrument in the first days of flight. When the failure occurred and the spacecraft was on the 33⅓-bits/sec telemetry rate, the time between voltage measurement samples was not sufficient to allow discharging down to the next lower consecutive voltage step. This was partially corrected when the bit rate was lowered to 8⅓ bits/sec. However, with the increasing time constant resulting from the lowered temperatures, the data again became unintelligible.

A series of radiation tests was performed on selected spacecraft subsystems in an attempt to determine their sensitivity to intense radiation fields. Subsystems such as the Canopus tracker, data encoder, gyro electronics, scan system, TV, and planet sensors were tested. The results indicated the spacecraft electronics lower sensitivity limit to be 2 to 3 orders of magnitude greater than the best available estimates of the maximum Mars field intensities that may be expected.

Nine encounter tests were conducted using the *Mariner* proof test model, simulated data, and the flight spacecraft as the data source. These tests were intended to exercise the Space Flight Operations System operational and technical personnel in the system and procedures to be used during the encounter phase of the mission. The encounter plan is as follows: The encounter sequence will begin about 2 hr before the *encounter sequence start* command MT-7 is issued. The scan platform will be prepositioned at an optimum scan angle for TV pictures.

Then, backup ground commands will be sent to ensure starting and stopping of the tape recorder. These commands will be timed to arrive at the spacecraft shortly after the nominal narrow-angle acquisition time (start of the tape recorder) and after the second end-of-tape signal from the tape recorder (stopping of tape recorder).

### C. Mariner IV Radio Subsystem Performance

The *Mariner IV* radio subsystem (Fig. 1) consists of a phase-coherent transponder designed for maximum reliability through the independent use of redundant exciters and power amplifiers. A phase-modulated RF signal may be either received or transmitted by the spacecraft on a directional antenna or low-gain antenna, depending upon

spacecraft orientation and operational mode. Diplexing of the signals on either antenna is accomplished through the use of circulator switches.

The received signal is coherently detected by means of a phase-locked automatic-phase-control (APC) loop in the transponder receiver, the output being the modulated command subcarrier that is appropriately fed to the command subsystem for further processing. When the transponder APC loop is in lock, the receiver local oscillator also serves as the transmitter frequency controlling element. When the APC loop is out of lock, transmitter frequency control is transferred to a fixed crystal oscillator. Thus, when the receiver APC loop is in lock, the signal transmitted from the spacecraft is translated in frequency and phase from the ground signal, but is coherent with it.

The *Mariner IV* radio subsystem has operated continuously with no evidence of any malfunction or performance degradation. The following anomalies were observed: (1) traveling wave tube helix current variation, (2) interferometer effect observed as amplitude variations of the

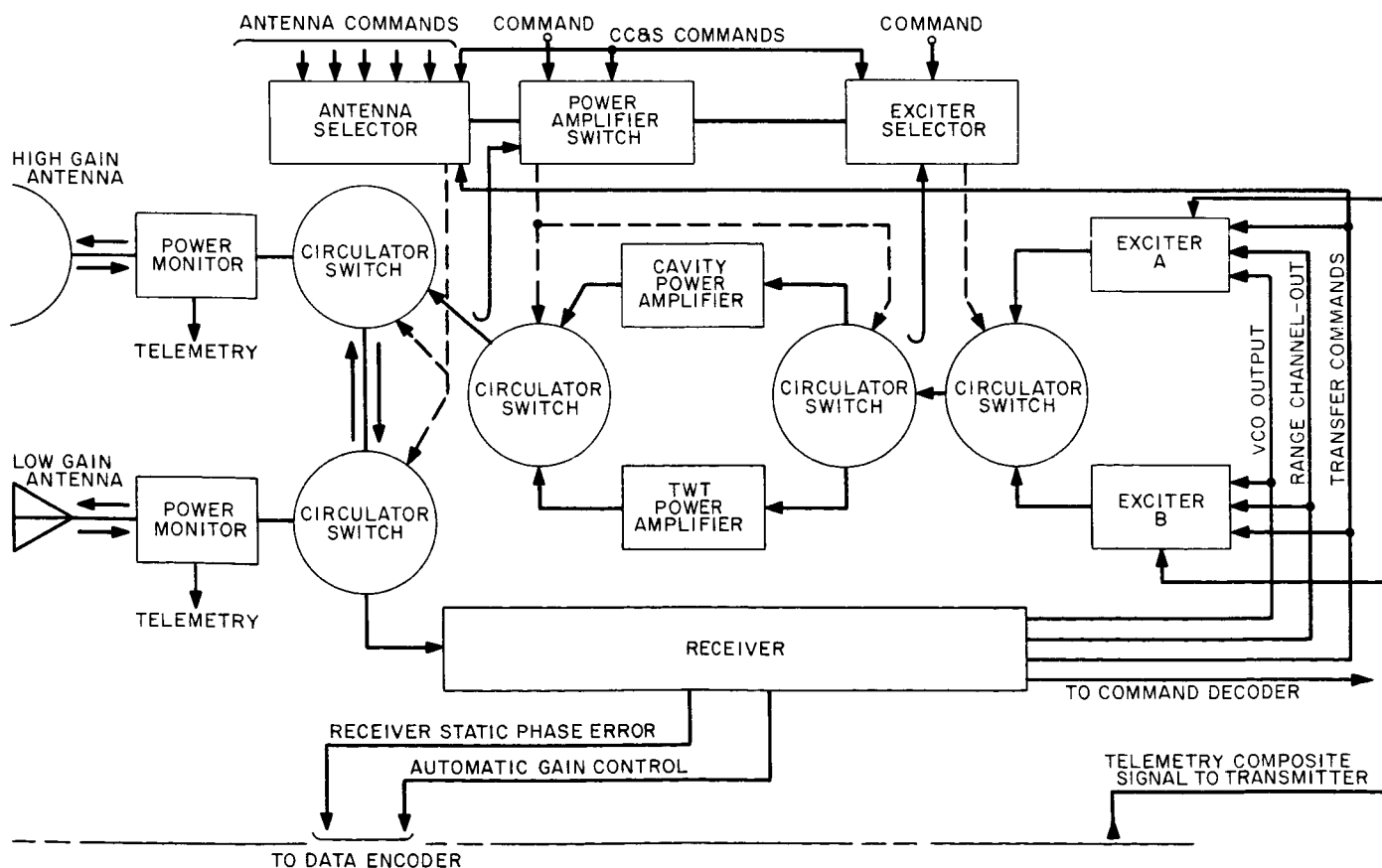


Fig. 1. Mariner IV radio subsystem

signal, and (3) slight frequency shift while in one-way lock. Each of these is well-understood and can be considered characteristic of this type of system.

The best lock frequency is the frequency onto which the spacecraft APC will lock in minimum time. It also corresponds to the average frequency at which the receiver voltage-controlled oscillator (VCO) operates when out of lock. Due to aging and temperature differences, the best lock frequency may change during flight. Therefore, two methods are being used to continuously update the estimate of the best lock frequency: (1) the direct measurement, by the Deep Space Instrumentation Facility (DSIF), of the frequency giving the shortest lockup time, the only requirement being that the DSIF tracking sta-

tions follow certain procedures to acquire two-way lock; and (2) the recording of spacecraft static phase error telemetric values when out of lock and the subsequent averaging of the spacecraft static phase error readings over a sufficiently long period of receiver out-of-lock condition. The average telemetric value can then be converted to spacecraft VCO frequency from the appropriate calibration table.

Using the updated best lock frequencies, ground stations have repeatedly obtained two-way lock with the spacecraft within a few seconds after the signal arrived at the spacecraft. Prior to the use of the updating techniques, it occasionally took more than 1 hr to obtain two-way lock.

# DEEP SPACE NETWORK

## IV. Deep Space Instrumentation Facility

### A. Introduction

The Deep Space Instrumentation Facility (DSIF) utilizes large antennas, low-noise phase-lock receiving systems, and high-power transmitters located at stations positioned around the Earth to track, command, and receive data from deep space probes. The DSIF stations are:

Station	Location
Goldstone Pioneer	Goldstone, California
Goldstone Echo	Goldstone, California
Goldstone Venus (research and development)	Goldstone, California
Goldstone Mars (under construction)	Goldstone, California
Woomera	Island Lagoon, Australia
Tidbinbilla	Canberra, Australia
Johannesburg	Johannesburg, South Africa
Madrid	Madrid, Spain
Spacecraft Monitoring	Cape Kennedy, Florida
Spacecraft Guidance and Command (under construction)	Ascension Island

To improve the data rate and distance capability, a 210-ft-diameter Advanced Antenna System is under construction at the Goldstone Mars Station, and two additional antennas of this size are planned for installation at overseas stations. Overseas stations are generally operated by personnel of the respective countries.

It is the policy of the DSIF to continuously conduct research and development of new components and systems and to engineer them into the DSIF to maintain a state-of-the-art capability.

### B. Tracking Stations Engineering and Operations

#### 1. Goldstone Pioneer Station

Tracking for the *Mariner IV* mission progressed satisfactorily during this reporting period. The prototype S-band system has been in continual operation since the launch of *Mariner IV*, except for the brief period when the antenna was used with the L-band system for *Ranger VIII* and *IX* tracking. Early in the *Mariner IV* track, the operation became routine; periodically, as the distance to the spacecraft increased, a command loop between the Goldstone Pioneer Station and the spacecraft was established for training operations and for providing a continuous tracking capability.

The original S-band system at Pioneer used for the *Mariner IV* track and the Tidbinbilla and Madrid Tracking Stations' S-band systems have completed testing. The Ascension Island and Woomera Tracking Stations' S-band systems are in the process of installation and testing. Personnel who will install and operate the S-band equipment at Woomera are at the Pioneer Station for training in the installation, operation, and maintenance of the system. The training is to be augmented by practical experience with the *Mariner IV* operations during a scheduled track of the spacecraft.

Installation of the ground support system for the *Surveyor* Project is continuing. Tests of the command and data handling console and the interfaces with the Pioneer Station digital instrumentation equipment have been completed. Compatibility tests between the *Surveyor* equipment and the S-band system were conducted during the times that the Pioneer Station was not involved in actual *Mariner IV* tracking. An enlarged screen room was erected at the Goldstone Microwave Test Facility for installation of a *Surveyor* test model, which will be used in simulated flight, lunar landing, and postlanding tests. The Pioneer Station S-band equipment and the *Surveyor* ground control equipment will be used for these tests.

The 30-ft az-el mockup antenna at the Pioneer Station is nearing completion. Static equipment installations will be performed on this antenna for determination of mounting and location.

## 2. Goldstone Echo Station

The installation of the Echo Station S-band system was completed in June, except for certain interfaces with the

digital instrumentation equipment. System tests will be performed until approximately July 6, at which time the Echo Station will operate as a backup to the Pioneer Station for *Mariner IV* tracking.

During the conversion from L- to S-band, all cabling associated with L-band was removed from the control room and the antenna, and new cabling was installed. The recabling included the S-band klystron coolant lines, the traveling wave maser cryodyne lines, and all electronic signal and control lines. All cryodyne lines were pressure-tested with a series of sustained operations in both static and dynamic conditions. Because time requirements for *Mariner IV* backup precluded installation of the standard declination wheel equipment room, one of the equipment cages on the antenna was reworked for the receiver assemblies, and the transmitter was mounted in the same location as the L-band transmitter. Otherwise, the antenna remained unchanged. The new S-band electronics equipment was installed in its permanent configuration in the control room (Fig. 1).

The *Pioneer* probe ground control equipment was installed in the control building. Interface tests between the *Pioneer* probe mission-dependent equipment, the digital instrumentation equipment, and the analog instrumentation equipment were conducted, including a test run of a taped simulated *Pioneer* tracking mission. Additional testing with the S-band system was scheduled for those times between system tests, *Mariner IV* testing, and backup tracking support.

Implementation of a Goldstone Primary and Secondary Standards Laboratory has begun at the Echo Station.



Fig. 1. Goldstone Echo Station S-band control room



Traceable to the National Bureau of Standards, the Primary facility will perform calibrations of inspection, testing, and laboratory-working-level equipment, tools, and devices. Standards equipment used by the overseas DSIF stations and the Spacecraft Monitoring Station will be certified by this laboratory.

### 3. Goldstone Venus Station

Since May 1, the Venus Station has been operational in a transmit-command capacity for *Mariner IV* backup support. During scheduled weekly operations, two-way coherent doppler and three-way noncoherent doppler were established between the Goldstone Pioneer Station and the Venus Station, and three-way noncoherent doppler between the Pioneer, Venus, and Tidbinbilla Tracking Stations. Although original plans called for a high-power command capability for *Mariner IV* backup (SPS 37-28, Vol. III, pp. 12, 13), the Venus Station 100-kw cone transmitter assembly was modified to include a 2295-Mc traveling wave maser. With associated conversion equipment, the Venus Station had the additional capability of receiving *Mariner IV* signals with the standard 2388-Mc receiver. Operation was limited to transmitting only, or to receiving only pending development of a 100-kw diplexer. The Venus Station provided

prime receive capability for reception of telemetry data during a planned 4-day shutdown of the Pioneer Station's maser. The receiver operated perfectly, and good telemetry data were received and transmitted to the JPL Space Flight Operations Facility by means of microwave link and the demodulation unit at the Pioneer Station.

The spectrum analysis and ranging experiments for Mars and Mercury were completed. Additional measurements of the temperature of Mars were made, and several measurements (at 2388 Mc) were made of temperatures of various radio star sources.

In a continuing effort to increase the operational capabilities of the 30-ft az-el antenna at the Venus Station (Fig. 2), modifications to the basic design have been incorporated. Most were implemented to provide a true operational scale model of the 210-ft Advanced Antenna System (AAS). These modifications were: (1) replacement of the feed support (quadripod) with a true  $\frac{1}{4}$ -scale model of the AAS quadripod, (2) provision of a precision  $\frac{1}{4}$ -scale model AAS subreflector and a precision hyperbola adjusting mechanism, and (3) replacement of the cable windup assembly with an upgraded design.

### 4. Madrid Tracking Station

Construction of the 85-ft polar-mounted antenna was recently completed, bringing the Madrid Tracking Station closer to operational status. The antenna incorporates such new DSIF features as an enclosed two-level electronics house, a truss quadripod, modified counterweight cages, air conditioning, an optical acquisition aid assembly, and a modified Cassegrain cone and hyperbola assembly. In addition, new high-performance S-band surface panels, increased hour-angle coverage, a four-legged pedestal and "beefed-up" structure for improved surface tolerance and over-all stiffness, and modified hour-angle and declination drive skids for improved adjustability and stiffness are provided.

### 5. Spacecraft Guidance and Command Tracking Station

The Spacecraft Guidance and Command Tracking Station will provide additional early tracking of a spacecraft after its launch from the Eastern Test Range and prior to its acquisition by one of the standard DSIF stations. S-band equipment for the station is being assembled and tested at the Goldstone Pioneer Station by Ascension Island personnel. A full 10-kw 2115-Mc transmitting capability utilizing a 30-ft az-el antenna will be incorporated.

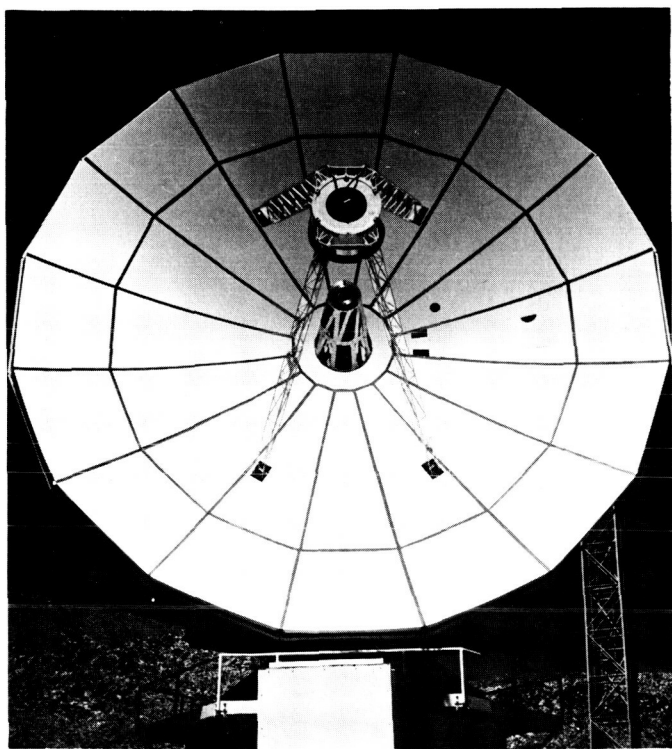


Fig. 2. Goldstone Venus Station 30-ft az-el antenna

Received spacecraft telemetry and antenna tracking data will be transmitted to the Spacecraft Monitoring Station and then to the JPL Space Flight Operations Facility in real time.

The design for the acquisition aid antenna system for this station (SPS 37-33, Vol. III, pp. 26-32) has been completed. The system consists of two antennas: (1) a low-gain horn monopulse tracking antenna to be located at the 30-ft antenna apex, and (2) a low-gain, 10-kw transmitter horn to be located on the 30-ft antenna surface. The monopulse tracking antenna equipment and a complete and tested transmitter horn antenna will be delivered to the Goldstone Pioneer Station 30-ft antenna mockup for mechanical assembly in early July.

## C. Developmental and Testing Activities

### 1. Digital Instrumentation Subsystem

The basic digital instrumentation subsystem (DIS) is composed of an SDS 910 computer, an SDS 920 computer, and their associated peripheral and data-gathering equipment. Each computer and its associated peripheral equipment form a completely independent subsystem. In the event of a failure in any portion of one subsystem,

the alternate subsystem may assume the responsibility for performing assigned tasks on a priority basis.

The initial configuration of the DIS previously reported in SPS 37-16, -20, -21, Vol. III, has recently been upgraded and now provides identical peripheral equipment for the SDS 910 and SDS 920 portions, the data-gathering equipment being common to, and addressable by, both units. During the second phase, computer-oriented equipment and a communications capability will be added.

To contain the additional elements, the subsystem has been increased from seven to eight rack cabinets. The subsystem format has been modified accordingly to group equipment with their respective computers. Access to the subsystem control panel, the two computer control panels, and the input/output equipment was arranged for operator convenience. The eight cabinets, together with two communications buffer cabinets on the left side, are shown in Fig. 3.

### 2. Ground Instrumentation for the Mariner IV Occultation Experiment

The *Mariner IV* occultation measurements will differ from those ordinarily made by the DSIF due to the short duration of the phenomena involved. The integration techniques normally used to obtain precise data cannot be applied in this experiment. To measure the occultation phenomena, two separate implementations will be employed.

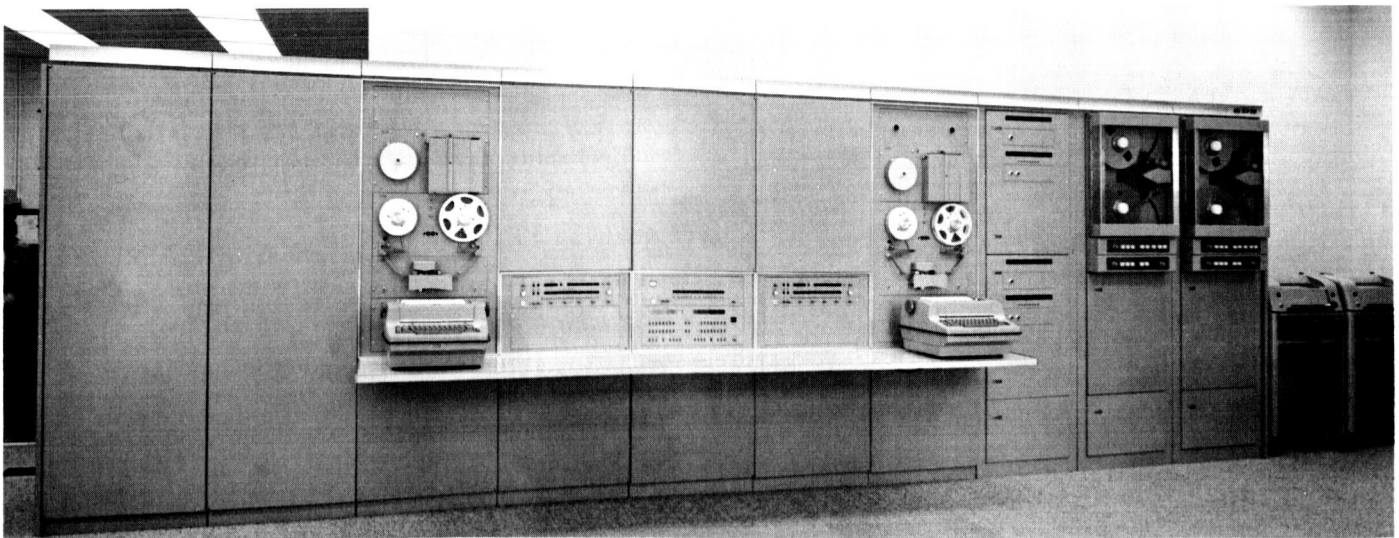


Fig. 3. Digital instrumentation subsystem

The first is the normal S-band configuration on receiver Channel 1. From this configuration, the received power as a function of time will be determined from the static and dynamic automatic gain control voltages. The doppler frequency will be obtained from the doppler extractor. To increase the resolution and decrease the quantization error, the normal doppler output will be multiplied by eight and will have its constant frequency bias removed.

The second channel will operate as an open-loop triple-conversion superheterodyne. All three local oscillator signals will be derived from the rubidium standard and synthesized to the required frequency. The output of the second channel will then be a frequency-translated amplified version of the S-band received signal, which will be in the 1- to 3-kc range at the output so that it can be predetection-recorded on magnetic tape.

The necessary modifications for the *Mariner IV* occultation experiment have been completed at the Goldstone Pioneer and Echo Stations.

### 3. 50-Mc IF Amplifier

Frequency modulation (FM) will be one of the methods used for transmitting information on the down-link signal for the Manned Space Flight Network. The information

to be sent by FM will be TV or analog data, voice, and telemetry. To accommodate the reception of the FM signals, a 50-Mc IF amplifier (Fig. 4) was developed for the ground receiver to increase the FM signals to the power level required by the demodulator. The amplifier was designed for a minimum half-power bandwidth of 10 Mc and a maximum gain of 40 db. A self-detection automatic gain control (AGC) system is incorporated within the amplifier module. The AGC system maintains the amplifier output signal level within 5 db of the nominal  $-20$  dbm over a 40-db dynamic range.

A series of tests were conducted on the receiver FM channel of the laboratory research and development system to evaluate the performance of the 50-Mc IF amplifier, using FM spectra of different modulating frequencies and indices over the range of receiver input signal levels. The primary purpose of the tests was to evaluate the AGC system in the FM channel. The first set of measurements was made using an unmodulated carrier to determine the effects of threshold noise; the second set was made on strong signals with an FM signal to determine the effect of a wide-band spectrum composed of discrete frequencies. It was found that, after the AGC is adjusted for a nominal  $-20$  dbm output level using an unmodulated carrier, variations in the output level resulting from a wide-band FM spectrum or noise will be less than 3 db. This value is within the design goal of 5 db.

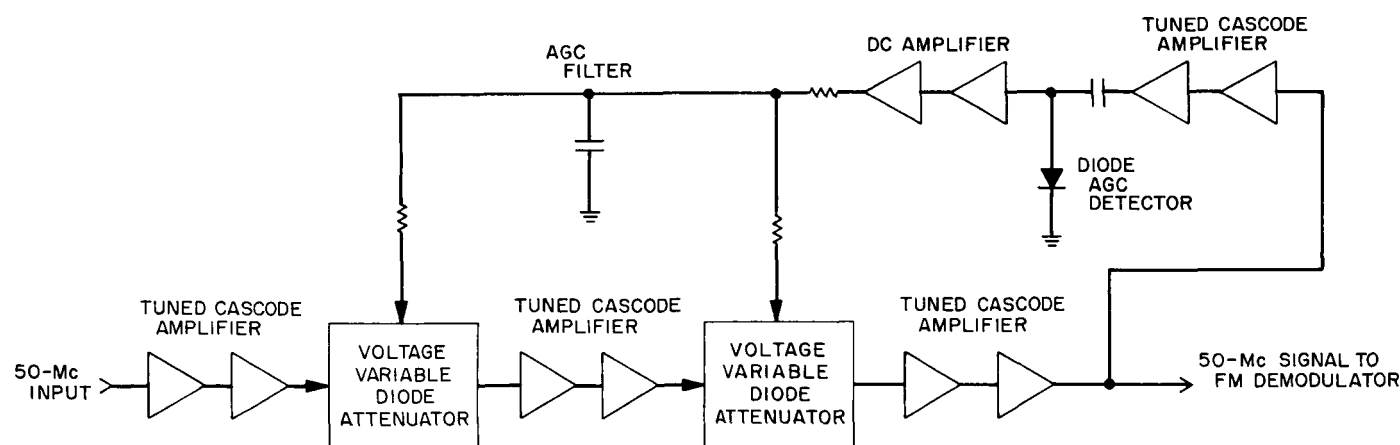


Fig. 4. 50-Mc IF amplifier block diagram

## SUPPORTING ACTIVITIES

### V. Environmental Test Facilities

#### A. A Preliminary Study of the Stability of a Multiple-Vibration-Exciter Control System

##### 1. Introduction

The use of a single exciter in the vibration testing of specimens is not always appropriate. Some objects, because of their weight, require large elaborate fixtures that contribute undesirable resonant responses of their own to the test results. Other specimens, because of their physical dimensions, cannot be adequately supported on a single vibration exciter, and undesirable cross axis acceleration is thus introduced. As a result, the use of multiple-vibration-exciter systems has been suggested.

The stability aspects of this technique must be considered. Specifically, if four separate stable control systems are connected in parallel to a common load, will the over-all stability be comparable to that which could be realized if the four were operating individually? A preliminary theoretical investigation of this problem is presented here, using matrix notation and a specific case:

a nonresonant load. A general method for analyzing multiple-vibration-excited systems with complex resonant loads is also indicated.

The multiple system to be investigated is illustrated in Fig. 1. It was decided, for analysis purposes, to drive the system from a common generator and to use identical control systems, each of which are connected to a common load. Fig. 2 illustrates a setup where, by injecting transients (pulses) and observing the results on meters, the problem may be physically investigated.

##### 2. Analysis

Preliminary work suggested analyzing the open-loop transfer function of a single system and plotting, by conventional control methods, the data obtained. Then, a transfer function of the four systems in parallel would be computed, and these data would be plotted on the same graph as those from the single stable system. A direct comparison of the two curves could then be made to analyze such parameters as: (1) gain margin and crossover, and (2) phase margin and crossover. Fig. 3 is a simplified block diagram of a single exciter system with an automatic vibration exciter feedback control system.

$G_{1(s)}$ ,  $G_{2(s)}$ , and  $H_{(s)}$  are the transfer functions of the amplifier, shaker, and feedback control system, respectively.

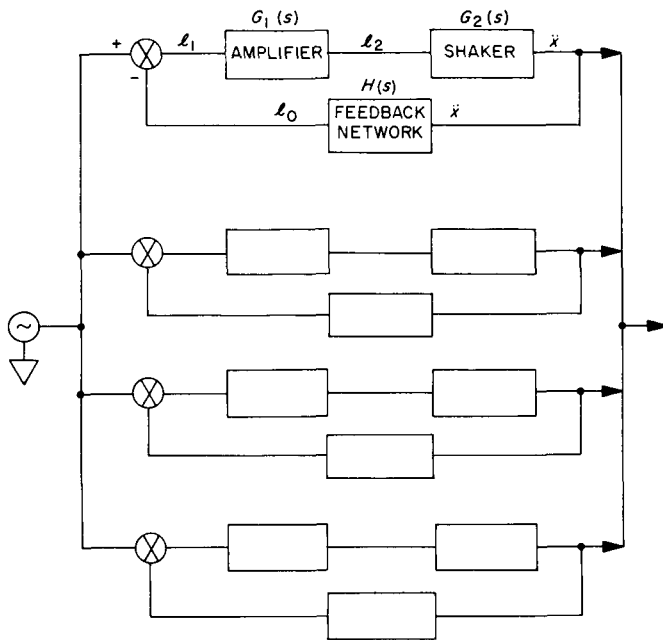


Fig. 1. Four-shaker system with common input and output

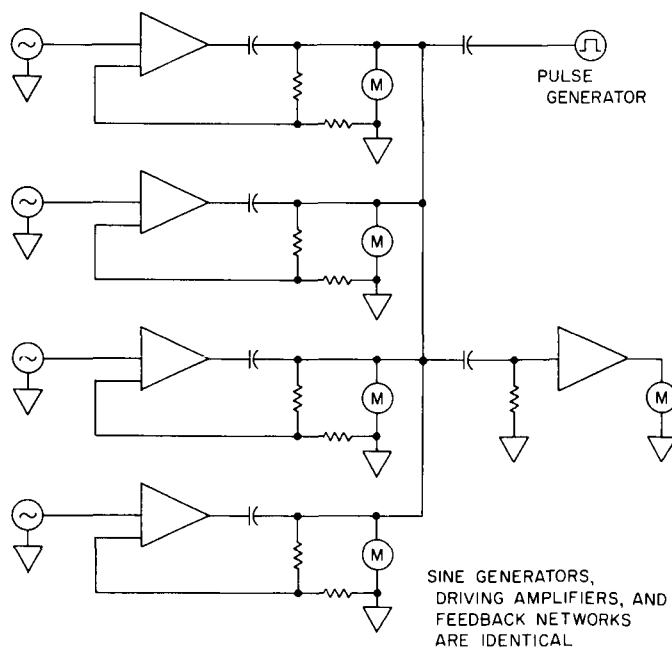
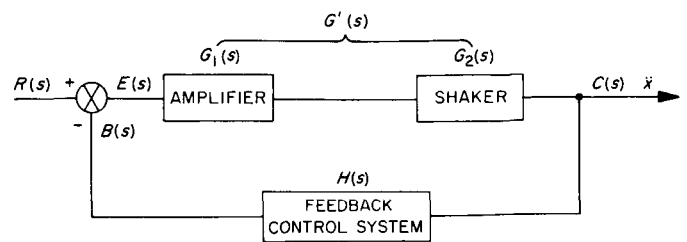


Fig. 2. Test setup for investigating the effects of a four-stage feedback control system on a common load



TRANSFER FUNCTIONS

$$\frac{C(s)}{R(s)} = \frac{G'(s)}{1 + G'(s)H(s)} \quad \text{CLOSED LOOP}$$

$$\frac{B(s)}{E(s)} = G'(s)H(s) \quad \text{OPEN LOOP}$$

$$\frac{C(s)}{E(s)} = G'(s) \quad \text{FORWARD}$$

Fig. 3. Single-shaker system using an automatic feedback control system

### 3. Procedure

The mathematical transfer function of the power amplifier and associated equipment was considered to be a constant; thus, constant voltage was assumed. The transfer function of the vibration exciter has been published by the manufacturer and is quite lengthy. The transfer function of the feedback control system was determined, since this information was not available. Thus, the open-loop transfer function could be obtained for a single system, but not for four systems in parallel.

### 4. General Matrix Solution

It was decided to express a single system in a  $[Y]$  admittance matrix; then, since the three other systems would be in parallel, the  $[Y]$  matrix of the over-all system could be obtained merely by adding the individual matrices; i.e., for parallel circuits,

$$[Y_{\text{total}}] = [Y_1] + [Y_2] + [Y_3] + \cdots + [Y_n].$$

There are many equivalent circuits for electromechanical vibration exciters that could be utilized in this analysis. In addition, a very simple equivalent circuit for the feedback control system was already known from the derivation of its transfer function. It was convenient to study the stability of the overall system by writing the equations of these analog circuits in matrix algebra form.

## 5. Conclusion

The following properties were used to conclude that multiple identical control systems, stable within themselves, driven from a common source, and attached to a nonresonant common load, will compose a stable system and that this stable system will, theoretically, be as stable as the individually stable systems.

- (1) It is assumed that an equivalent circuit of a single control system can be written and that the *nodal* equations of the circuit can also be written, thus obtaining the  $[Y]$  matrix.
- (2) The nodal equations of the circuit can be displayed as follows:

$$\begin{bmatrix} y_{11} & y_{12} & y_{13} \\ y_{21} & y_{22} & y_{23} \\ y_{31} & y_{32} & y_{33} \end{bmatrix} \begin{bmatrix} E_1 \\ E_2 \\ E_3 \end{bmatrix} = \begin{bmatrix} I_1 \\ I_2 \\ I_3 \end{bmatrix}.$$

- (3) Then, the  $Y$  matrix is defined as

$$\begin{bmatrix} y_{11} & y_{12} & y_{13} \\ y_{21} & y_{22} & y_{23} \\ y_{31} & y_{32} & y_{33} \end{bmatrix} = [Y_A],$$

where the terms  $y_{11}$ ,  $y_{12}$ , etc., are, in general, complex due to the mechanical-to-electrical analog.

- (4) Since all the systems are assumed to be identical, their  $[Y]$  matrices will be the same as  $[Y_A]$ ; i.e.,

$$[Y_A] = [Y_B] = [Y_C] = [Y_D].$$

- (5) It can be shown that, for the above general  $Y$  matrix,

$$\frac{E_1}{E_3} = \frac{E_{out}}{E_{in}} = \frac{\Delta y_{13}}{\Delta y_{11}}$$

is the transfer function if  $I_2 = I_3 = 0$  (ideal condition), where  $\Delta y_{13}$  and  $\Delta y_{11}$  are the cofactors of the  $y_{13}$  and  $y_{11}$  terms, respectively; i.e.,

$$\Delta y_{13} = \begin{vmatrix} y_{21} & y_{22} \\ y_{31} & y_{32} \end{vmatrix},$$

$$\Delta y_{11} = \begin{vmatrix} y_{22} & y_{23} \\ y_{32} & y_{33} \end{vmatrix}.$$

Therefore, the open-loop transfer function of a single system  $Y_A$  is

$$G_{(s)}H_{(s)} = \frac{\Delta y_{13}}{\Delta y_{11}} = \frac{\begin{vmatrix} y_{21} & y_{22} \\ y_{31} & y_{32} \end{vmatrix}}{\begin{vmatrix} y_{22} & y_{23} \\ y_{32} & y_{33} \end{vmatrix}}.$$

- (6)  $[Y]$  matrices add when in parallel; i.e., the sum of  $[Y_A] + [Y_B]$  is

$$\begin{bmatrix} y_{A11} + y_{B11} & y_{A12} + y_{B12} & y_{A13} + y_{B13} \\ y_{A21} + y_{B21} & y_{A22} + y_{B22} & y_{A23} + y_{B23} \\ y_{A31} + y_{B31} & y_{A32} + y_{B32} & y_{A33} + y_{B33} \end{bmatrix}$$

and similarly for adding  $[Y_C]$  and  $[Y_D]$ . Therefore,

$$[Y_{total}] = \begin{bmatrix} 4y_{A11} & 4y_{A12} & 4y_{A13} \\ 4y_{A21} & 4y_{A22} & 4y_{A23} \\ 4y_{A31} & 4y_{A32} & 4y_{A33} \end{bmatrix} = 4[Y_A];$$

i.e., the product of a matrix  $[Y_A]$  and the scalar 4 is the matrix  $4[Y_A]$  whose elements are the elements  $y_{ij}$  of  $[Y_A]$  each multiplied by 4.

- (7) There is a theorem in matrix and determinant algebra which states that, in effect, the matrix is left unchanged by the multiplication of each element of a row (or column) by the same nonzero constant; i.e., the transfer function of  $[Y_A]$  is the same as the transfer function of  $[Y_{total}]$ . This can be demonstrated as follows:  $G_{(s)}H_{(s)}$  for a single system  $A$  is

$$\frac{\begin{vmatrix} y_{A21} & y_{A22} \\ y_{A31} & y_{A32} \end{vmatrix}}{\begin{vmatrix} y_{A22} & y_{A23} \\ y_{A32} & y_{A33} \end{vmatrix}}.$$

$G_{(s)}H_{(s)}$  for the total parallel system is

$$\frac{\begin{vmatrix} 4y_{A21} & 4y_{A22} \\ 4y_{A31} & 4y_{A32} \end{vmatrix}}{\begin{vmatrix} 4y_{A22} & 4y_{A23} \\ 4y_{A32} & 4y_{A33} \end{vmatrix}},$$

which is simply

$$\frac{4 \begin{vmatrix} y_{A21} & y_{A22} \\ y_{A31} & y_{A32} \end{vmatrix}}{4 \begin{vmatrix} y_{A22} & y_{A23} \\ y_{A32} & y_{A33} \end{vmatrix}},$$

and the 4s cancel, leaving the same transfer function as that for any one of the individual systems. A simple example of this is given below: Consider the matrix

$$[Y] = \begin{bmatrix} 1 & 2 & 3 \\ 3 & 1 & 2 \\ 2 & 1 & 1 \end{bmatrix}$$

for which

$$\frac{\Delta y_{13}}{\Delta y_{11}} = \frac{(3 \times 1) - (2 \times 1)}{(1 \times 1) - (1 \times 2)} = \frac{3 - 2}{1 - 2} = -1.$$

Now, if all terms in the  $[Y]$  matrix are multiplied by 4, i.e.,

$$4[Y] = \begin{bmatrix} 4 & 8 & 12 \\ 12 & 4 & 8 \\ 8 & 4 & 4 \end{bmatrix},$$

$$\frac{\Delta y_{13}}{\Delta y_{11}} = \frac{(12 \times 4) - (8 \times 4)}{(4 \times 4) - (4 \times 8)} = \frac{48 - 32}{16 - 32} = -1.$$

The above analysis is limited by its own simplifications, assumptions, and equivalent circuits. It was found that, to obtain the forward transfer function of a single system, it was necessary to first consider the  $A$  matrix (or  $ABCD$  matrix) so that the multiplication of each transfer function in a single system could be performed by multiplying the series  $A$  matrices until the entire open-loop circuit was accounted for; then the  $A$  matrix could be converted to a  $Y$  matrix.

One advantage in using the  $[Y]$  matrix for analysis is that, if the system is changed or modified, only certain terms in the matrix need be changed; i.e., one doesn't have to write new equations each time a change (e.g., a load change) is made. This fact suggests an orderly approach to a more complex analysis, such as that of resonant loads using matrix notation.

## B. Special Equalization Procedure for Random Vibration Testing

The dynamic resonances of a specimen to be vibration-tested must be carefully considered. Mechanical gains or

losses due to resonance must be compensated for to prevent testing at levels above or below the test-specification parameters. The vibration exciter armature, the test adapter fixture, and the test specimen are always equalized as a system.

A unique equalization procedure was recently developed for random noise vibration tests performed on three "live" 800-lb solid-propellant motors at the JPL Environmental Facility for Hazardous Tests at Edwards Test Station. This technique minimized equalization time and permitted closer adherence to test-specification requirements than had previously been possible.

A preliminary specification-level vibration test was performed on an inert motor. Accelerometers were located at appropriate positions for vibration test monitoring (Fig. 4). The accelerometer data indicated system dynamic

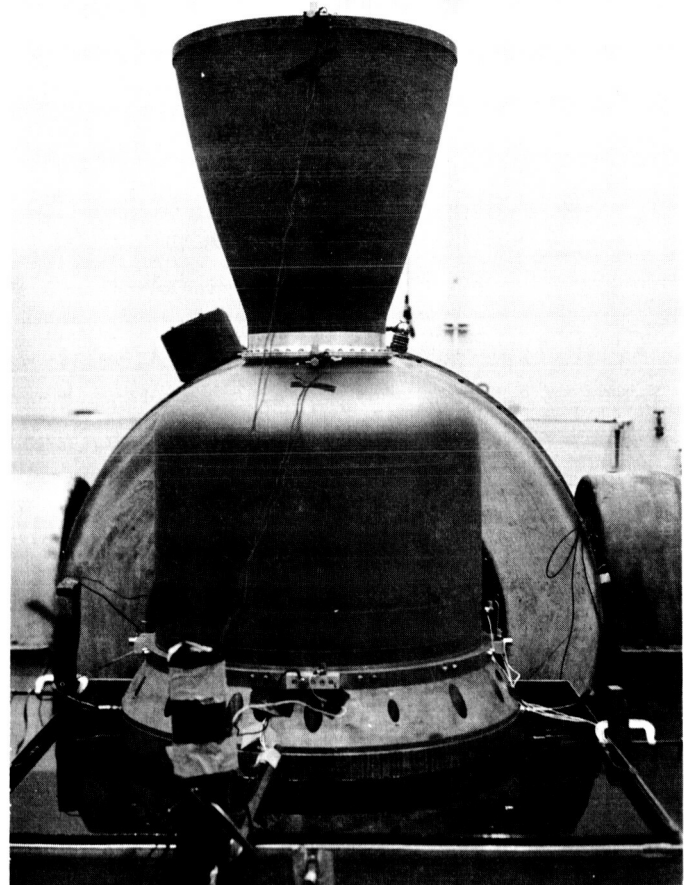


Fig. 4. "Live" motor vibration test setup with accelerometers in place

nonlinearities at motor resonance, and an investigation was conducted to locate the problem. It was found that a 1-g-rms sinusoidal input (20 to 2000 cps) resulted in a response similar in shape to the full-level unequalized noise input (Fig. 5), except for small frequency differences in the motor's fundamental resonant frequency range. This nonlinearity was also evident when a 2-g-rms sinusoidal sweep was compared with the 1-g-rms sweep (Fig. 6). Subsequently, the procedure for equalization described here evolved, resulting in consistent, accurate random vibration tests for the three solid-propellant motors.

The motor test setup was first subjected to a 1-g-rms sinusoidal vibration sweeping from 20 to 2000 cps (the spectrum of the test specification). The output of the control accelerometer (located on the fixture adjacent to the motor attachment ring) was maintained at the 1-g level while the input voltage required was plotted on

semi-logarithmic chart paper. The system was then exposed to a 2-g-rms sinusoidal vibration, servo-sweeping from 40 to 200 cps, while the required input voltage was plotted on the same chart used for the 1-g-rms level recording. The differences between the two plots resulted from system nonlinearities in the motor's fundamental resonant frequency range (40 to 200 cps). These plots were then used as the basis for equalizing the system. Ten peak and notch filters and a graphic equalizer were employed to fulfill this requirement (Fig. 7).

The motor was then subjected to an open-loop 10-sec full-specification-level (equalization circuits, in effect) burst of random noise. The output of the monitoring accelerometer was recorded on tape, and a tape loop containing 7 sec of the monitored signal was made. A 5-cycle analysis of the power spectral density was plotted at the test site and examined by the cognizant engineer for approval and verification of effective equalization

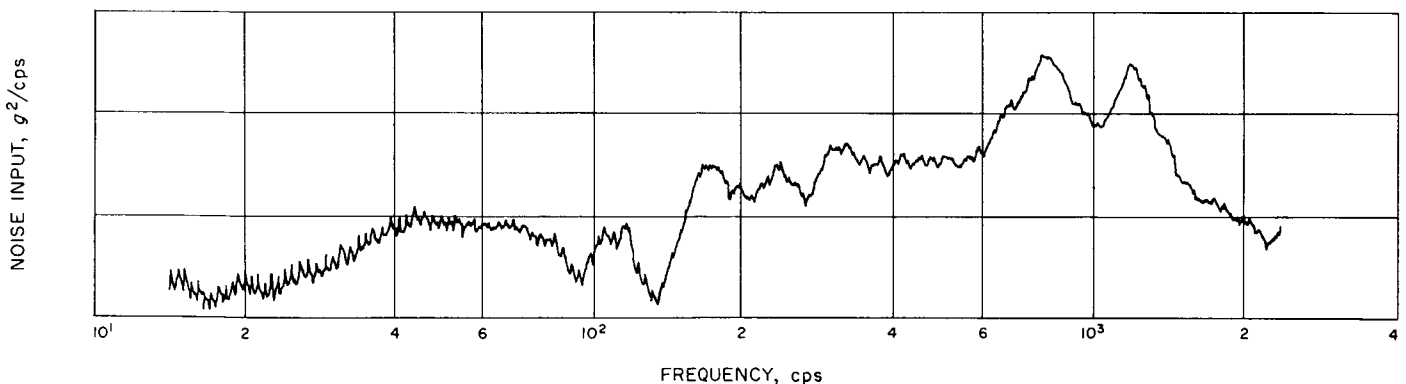


Fig. 5. Full-test specification-level unequalized noise input

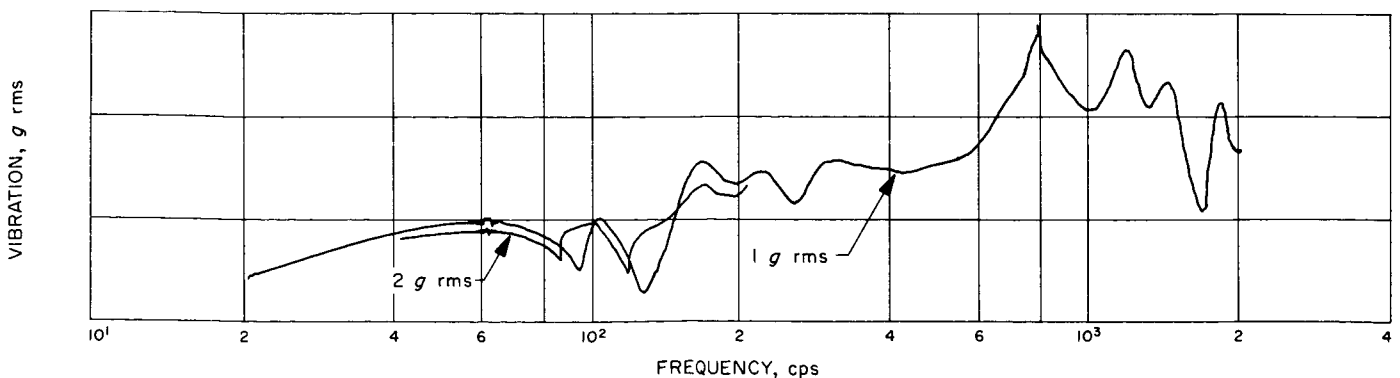


Fig. 6. Equalization-requirement sinusoidal sweep (1 and 2 g rms)



(Figs. 8 and 9). With this procedure, approved equalization was obtained for the three "live" motors with only *one* full-level 10-sec burst of noise required in each plane.

In conclusion, the advantages of this equalization procedure are as follows:

- (1) The test specimen is not unnecessarily exposed to an excessive time of high-level vibration while equaliz-

ing. This is a significant consideration for all specimens, and particularly for volatile and/or explosive test units.

- (2) The test equalization and results can be verified immediately at the test site.
- (3) Test specification tolerances can be more rigidly adhered to than was possible with previous equalization procedures.

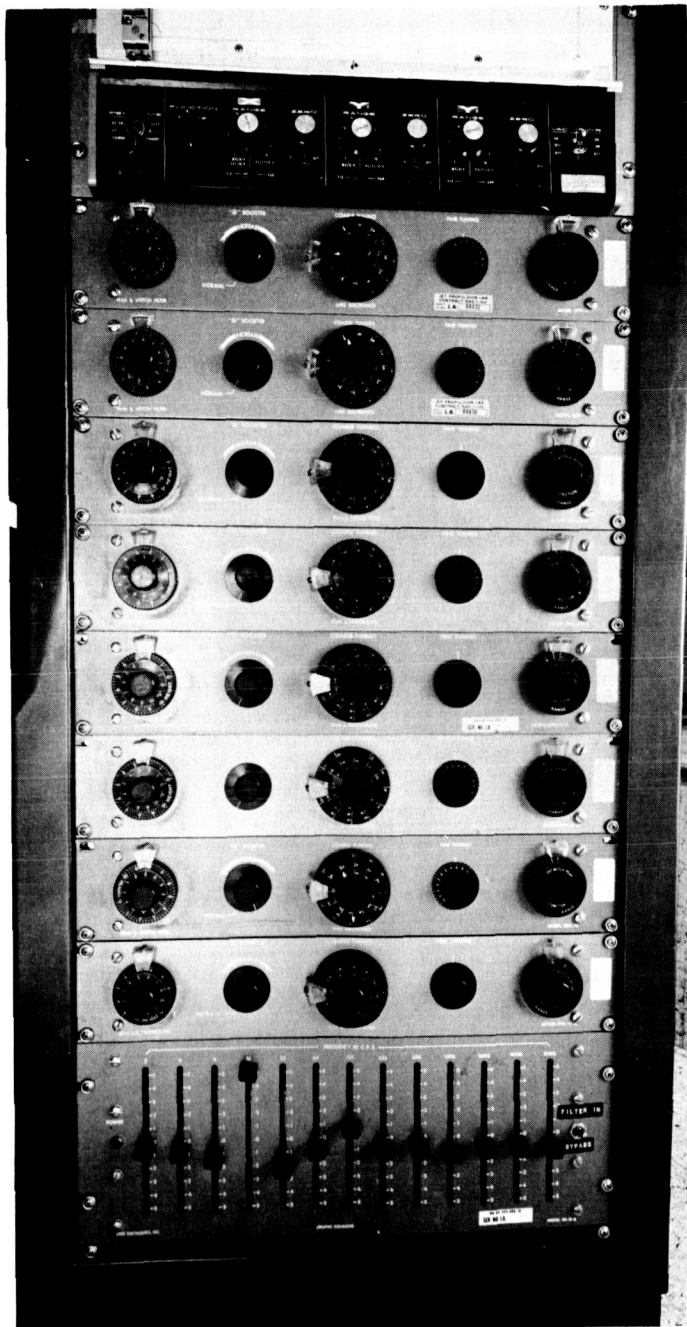
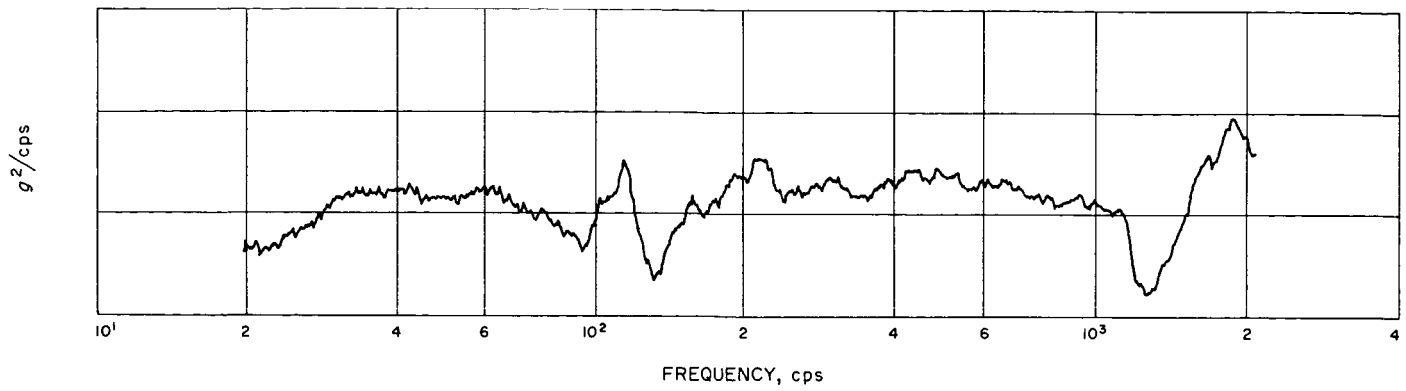
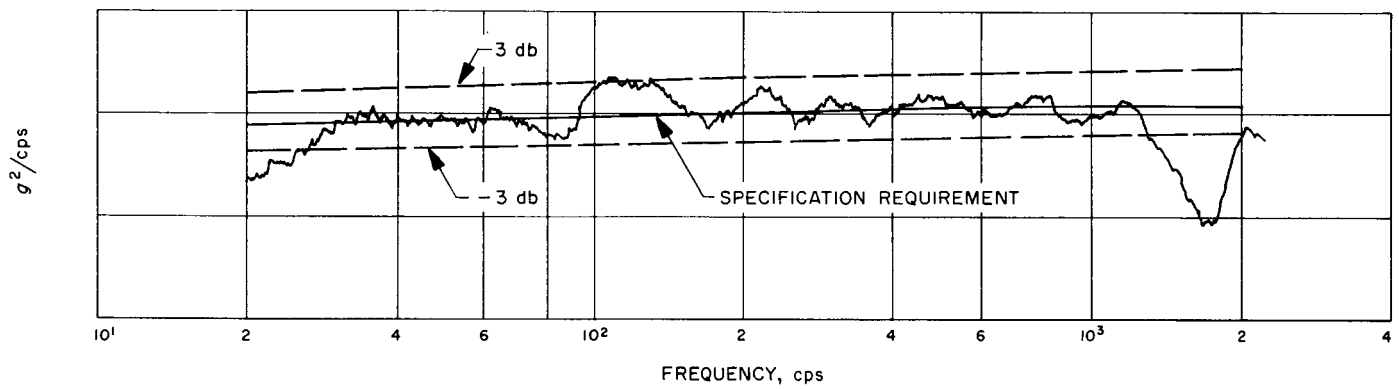


Fig. 7. Peak and notch filters and graphic equalizer



**Fig. 8. Power spectral density plot without equalization compensation**



**Fig. 9. Equalization-compensated power spectral density plot showing specification requirements**

## SPACE SCIENCES

## VI. Space Instruments

A. *Mariner IV* Ionization Chamber Failure Analysis

The *Mariner IV* ionization chamber performed nominally through the first 70 days of the mission. During this period, a profile of radiation intensity was faithfully recorded by the instrument as the spacecraft passed through each of the Van Allen belts, through the boundary of the magnetosphere, and into the relatively stable interplanetary region. Sixty-nine days after the mission began, a solar flare occurred. Both the ion chamber and the Geiger-Mueller (G-M) tube recorded peak activity of the flare. As the flare subsided and the ion chamber returned to the normal background level, the G-M tube indicated a slightly higher rate than expected over the downward trend, leveling off at a value approximately 30% above the expected preflare level. On the 84th day of the mission, after about 10 days of comparatively stable operation at this slightly anomalous level, the G-M tube rate rose sharply from approximately 40 to 18,000 counts/sec, indicating a spontaneous self-sustained discharge.

On the 109th day of the mission, the G-M tube rate dropped to zero and the ion chamber interval became infinite. No response from either sensor has been observed since then.

It was calculated that the G-M tube had first failed (by spontaneous discharge) after having counted  $\sim 8 \times 10^8$  counts, after expending only 8% of its rated  $10^{10}$  count life. In an attempt to understand this phenomenon, ten tubes were taken from the batch from which the flight tubes were selected. Seven tubes were operated at various fixed count rates until such time as each tube failed by continuous discharge. Three tubes were exposed to the higher flux levels, but without power applied. No significant shift in the voltage plateaus of these latter tubes was observed.

The tentative conclusion from the results obtained was that the total life count of a tube depends upon the rate at which the tube counts: the higher the count rate, the more counts a tube will assimilate before the onset of spontaneous discharge. Since each pulse is smaller at higher rates, it is likely that the tubes fail by spontaneous

discharge after a certain amount of charge has passed through them. It also appears that the tube selected for *Mariner IV* may have been an especially short-lived tube in spite of the excellent stability displayed in selection and prelaunch tests. It appears that any other tube in the batch would have had a sufficient life-count capacity to complete the mission.

It was speculated that the quench gas, a mixture of chlorine and silicon-tetrafluoride, was depleted. This would explain the sustained count rate in the absence of sources. Good tubes and failed tubes were submitted to the JPL Chemistry Section 326 for analysis and comparison. Analysis of the filling gas as performed by a mass spectrometer indicated no significant differences between gas from good tubes and gas from expended tubes. However, this test was deemed inconclusive due to the poor sensitivity of the available spectrometer. Gas samples have been submitted for further analysis and comparison on a spectrometer with improved sensitivity.

A darkening of the transparent cathode of the failed tubes was noted as they were allowed to operate in the spontaneous counting mode. Chemical analysis of cathode washings showed chlorine, one of the quenching gases, to be present on the cathodes of both good and failed tubes.

The most significant and entirely unexpected finding occurred when the tin-oxide cathode of a blackened tube was carefully scraped and the scrapings were submitted for spectrographic analysis. Tests showed a remarkable 72% (by weight) tungsten content. The tungsten transport from anode to cathode is not yet fully understood.

The subsequent failure of the ion chamber portion of the instrument on the spacecraft, accompanied by the apparent simultaneous drop to zero in the G-M tube rate, indicated that perhaps the power supply, which is common to both detectors, had failed or had been shorted. This speculation was made more credible in view of the tungsten transport phenomenon. It was hypothesized that the anode may have been steadily weakened by the emission of tungsten until electrostatic attraction by the cathode was sufficient to break the anode. The slender anode might be attracted to the cathode to the extent that physical contact might be made, the ensuing arc providing the energy necessary to weld the anode to the cathode, resulting essentially in a short circuit of the power supply. In order to provide a method of quickly testing the hypothesis, it was necessary to sever the anode of the tube while the tube was counting normally under high voltage. To accomplish this, a good tube was

mounted to the breadboard circuit. By means of optical lenses, the beam from a ruby laser was focused through the glass envelope of the tube onto the anode. With the tube in normal counting operation and powered by the breadboard ion chamber circuit, the laser was pulsed. The anode burned in two and the energized segment was attracted to the cathode. However, the anode did not weld to the cathode immediately, but required a period of approximately 40 min, during which time the arcing between the electrodes was visible through the glass tube. Possibly the reason the welding was not instantaneous, but may have been instantaneous with the unit in space, was because burning the anode in half resulted in the formation of a small ball of tungsten on the melted ends of the anode. The additional mass, slightly larger than the diameter of the anode wire, might be expected to require considerably more energy for welding than an anode wire eroded to the breaking point by tungsten emission. Also, an eroded wire might have significantly less restoring force to counter the electrostatic attraction.

Additional evidence in favor of the shorted power supply hypothesis occurred when the life test unit failed in a manner much the same as the *Mariner IV* instrument. The G-M tube output dropped to zero after a count rate profile and a time interval comparable to that of the spacecraft instrument. Simultaneously, the test voltages at all monitor points dropped in a manner that suggested a shorted supply. However, the ion chamber sensor continued to function with only slight increase in the expected period as opposed to the immediate failure of the chamber in space. This apparent discrepancy in the failure modes seems to have been resolved by subsequent tests on the breadboard circuit. If the power supply is shorted through the G-M tube, breadboard tests indicate that the high voltage would decrease to a value below the ion chamber pulsing threshold if the life test unit (operating at ambient room temperature) were subjected to cold temperatures comparable to those experienced by the unit in space. It has been decided to await the end of the life test to verify this supposition, using the life test unit directly.

Further evidence for the postulated failure mode has recently been obtained. Three failed tubes functioning in their spontaneous discharge modes have successively been operated on the breadboard circuit until output from the tubes ceased. In all three cases when each tube finally quit producing the spontaneous output pulses, it was noted that the filaments had broken. In two of the tubes, the anode was observed to have been instantaneously welded to the cathode, resulting in a short circuit

of the power supply. The third tube proved to have an open circuit within the tube. This occurred because the break in the anode was so close to the glass feed-through sheath as to provide insufficient length for the energized end of the broken anode to reach the cathode.

In conclusion, there seems to be one bit of evidence that perhaps contradicts the proposed failure mode. Based on tests performed on the breadboard, it is calculated that, if a short occurred in the G-M tube as postulated, the energy dissipated by the instrument should have increased by approximately 65%. Personnel from the thermal control area feel that such a step function increase in dissipated power would be detectable in the instrument's thermal performance. A review of thermal data from the instrument during the time in question does not indicate any obvious change in dissipated power. However, it is admitted that, under certain conditions, a power dissipation increase might be masked. Investigation using the life test unit after life tests are completed may resolve this question.

## B. Mariner IV Plasma Probe Failure Analysis

### 1. Appearance of Problem

The Massachusetts Institute of Technology (MIT) plasma probe operated normally at the fast step rate (33½ bits/sec) for 7 days after the launch of the *Mariner IV* spacecraft. The instrument obtained many readings above the noise level, and the plasma data continuously exhibited a clearly defined spectrum of one and, occasionally, two peaks. Instrument calibrations indicated proper operation without exception.

The instrument generates a high voltage which is variable in 32 steps from 56 to 10,000 v, but only those steps corresponding to 4210 and 5050 v are monitored by the high voltage calibration. At 341:00:00 GMT, the high voltage calibration indicated high voltage failure by decreasing from normal to minimum over a 2-hr period. As the calibration readings neared minimum, the plasma readings decreased to the noise level of the instrument. Other instrument calibrations appeared normal and justified the opinion that the problem was confined to the high voltage section.

It was immediately concluded that an arc had developed in the high voltage circuit and that there was insufficient high voltage to make plasma measurements. The existence of arcing was supported by evidence of system disturbance from 341:02:00 to 342:03:00 GMT. Spacecraft data showed that data encoder deck skips occurred simultaneously with cosmic dust detector (CDD) hits. (There has been no evidence of a similar system transient since day 342.) The failure of R339 (Fig. 1) was considered and rejected. While the shorting of R339 would load down the high voltage, it would not necessarily produce RF noise, nor would it cause lower-than-normal high voltage calibrations. The opening of R339, a more likely mode of film resistor failure, would not lower the high voltage.

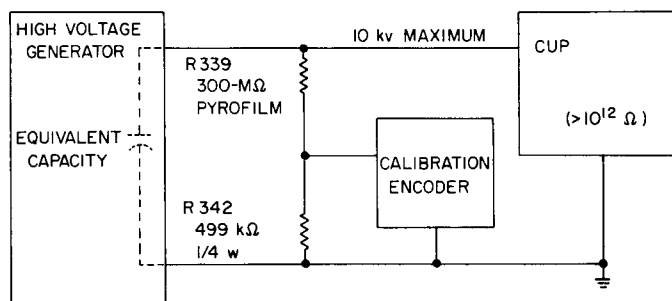


Fig. 1. Failed portion of plasma probe instrument

### 2. Arc Tests

The proof test model (PTM) probe was temporarily fitted with a spark gap during the last week of December. Bench operation showed that RF interference was being radiated directly and that it was present on the data readout line. When the instrument was mounted on the PTM spacecraft, data encoder deck skips and CDD hits were correlated with arcs at the spark gap. Thus, it was established that plasma probe arcing caused the system interference observed in the *Mariner IV* spacecraft.

### 3. Hypothesis

In a telephone conference of January 4, 1965, JPL was informed that a 300-MΩ resistor (R339) had opened in the life test being conducted at MIT. This information leads to the following hypothesis concerning the mode of failure:

- (1) The opening of R339 would cause the high voltage calibration to decrease to minimum since the resistor is the top leg of a voltage divider feeding the calibration circuit (Fig. 1).

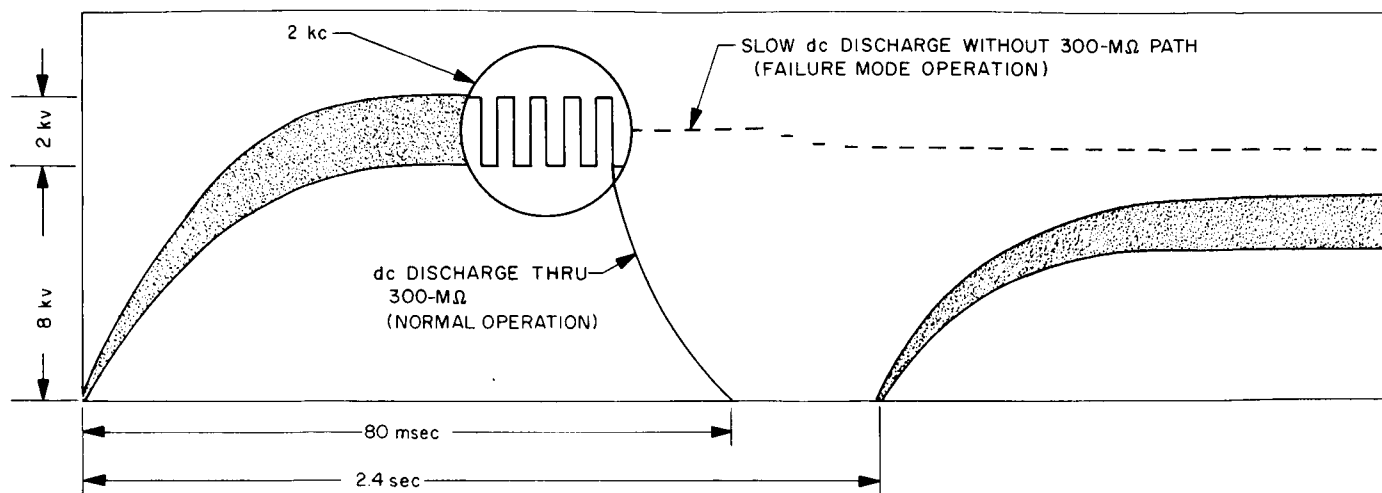


Fig. 2. Normal and failed high voltage waveforms

- (2) As seen in Fig. 2, the high voltage consists of 80-msec bursts every 2.4 sec at the high bit rate. The burst amplitude varies according to a pre-programmed pattern of 32 steps. At maximum output, there is a 2-kv peak-to-peak 2-kc square wave superimposed on 9 kv dc. At less than maximum output, the burst amplitude is less but the ratio of ac to dc is constant. At the end of the burst, the ac terminates abruptly, but the dc is stored in the capacitors of the high voltage generator and must discharge through R339 and R342 (Fig. 1). In the first burst of Fig. 2, the instrument would be measuring all plasma with an energy level lying between 8 and 10 kv. It is important to note that the instrument does not sense plasma lying outside the ac envelope and that high dc potentials permit only high energy plasma to be seen.

The opening of R339 would open the dc discharge path and result in the slow decay rate which is illustrated by the dashed lines in Figs. 2 and 3(a). Although the instrument would still go through its sequence of steps, the dc level would no longer follow the proper pattern, but would remain high and permit only the higher energy plasma to be seen. Furthermore, the calibration of the instrument would vary from step to step because the ac to dc ratio varies with each step. Therefore, the instrument sensitivity is reduced on all but the highest voltage step.

- (3) The opening of R339 could result in arcing either within the failed resistor or in some other part of the high voltage circuit. The tendency to arc externally would be increased by the presence of volt-

ages which are slightly higher than normal and which are maintained at high levels for much longer periods. It is known that arcing will occur under normal conditions if the high voltage generator is operated without the several picofarads of load capacitance presented by the cup.

#### 4. Support of Hypothesis

At first, MIT doubted that the opening of R339 was a likely cause of the *Mariner IV* plasma probe failure; it was felt that there would be enough leakage, especially in the back direction through the high voltage rectifiers, to provide an adequate discharge path for the dc. Subsequent tests at MIT and JPL proved that the presence of the resistor was necessary to provide an adequate discharge path and that, without the resistor, the dashed discharge curves of Figs. 2 and 3(a) would result. An examination of the MIT life test data revealed that R339 failed over a period of 6 hr in the life test at MIT. R339 was also found to be open in the PTM probe at JPL. The date of this failure is entirely unknown since the PTM is the one model which does not incorporate a high voltage calibration in accordance with Engineering Change Request (ECR) 6930. Without the incorporation of the ECR, no normal bench or systems test would indicate the failure of the resistor. All personnel associated with the plasma probe now concur that the failure on the *Mariner IV* was undoubtedly due to the opening of R339.

The failure of R339 is still the only phenomenon which can explain an anomaly found in the *Mariner IV* spacecraft data. Since December 6, 1964, *Mariner IV* data indicate that plasma is still occasionally measured, but only as the plasma steps are ascending. As seen in Fig. 3(a),

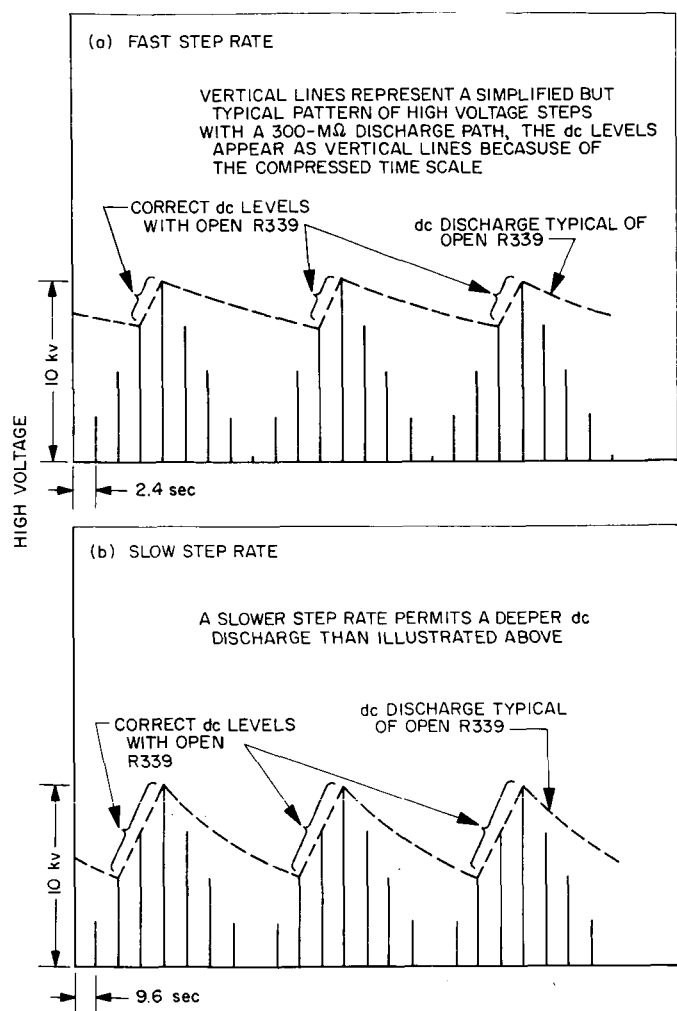


**Fig. 3. Effect of failure on spectral analysis**  
 (a) at  $33\frac{1}{3}$  bits/sec sampling rate  
 (b) at  $8\frac{1}{3}$  bits/sec sampling rate

the vertical lines represent the desired dc waveform for each high voltage burst. The opening of R339 causes the dc potential to follow the dashed line. As a result of the slow decay, the dc voltage is correct for only a few ascending steps. Since the ac and dc levels are correct for these bursts, the instrument will properly measure any plasma present in the corresponding energy levels. Little plasma will be seen in the remaining steps because the narrow ac window makes the instrument insensitive and the high dc potential limits the measurements to high energy plasma, which at present is relatively scarce.

A slower step rate will permit a deeper dc discharge, as shown in Fig. 3(b). With a deeper dc discharge, the correct voltages are established for a greater number of energy steps. Not only will there be a greater number

of correct measurements, but measurements will be made at low energy levels where more plasma has been seen. When the step rate was reduced on January 3, 1965, the *Mariner IV* spacecraft data showed an increase in plasma activity as predicted.

Since the dc discharge curve is established primarily by the leakage of the high voltage rectifiers, it varies greatly with temperature. In recent months, cooler instrument temperatures have reduced the rate of discharge to the point where very little plasma can be seen.

As instrument availability has permitted, dc discharge curves have been run at JPL and MIT on the remaining plasma probes. Since there is no reason to assume that the *Mariner IV* curve is atypical, a probable curve can be synthesized and used to recover some of the plasma information which came through from the defective instrument before cooler temperatures prevailed. An absolute calibration of the *Mariner IV* instrument will never be possible because the contributing parameters vary significantly from instrument to instrument.

Pyrofilm Resistor Company, the manufacturer of the R339, states that it is the presence of a radial ac field which causes resistor failure and that, furthermore, failure would be expected with the intensity of the field produced by the 2-kv burst. In the laboratory, it was observed that the field produced ionization within the resistor and gradually removed the carbon-film resistive element from its ceramic base. It is to be noted that the flight resistors successfully passed a screening procedure. Unfortunately, this procedure did not subject them to an ac stress.

## C. *Mariner IV* TV Interpretation Studies

In the period between launch and the return of TV picture data, members of the scientific team responsible for evaluation of the pictures are becoming familiarized with the capabilities and limitations of the spacecraft TV subsystem as compared with standard Earth-based and Earth-satellite-based TV and photo-reconnaissance devices. The problem of interpreting an unknown planetary surface has led to laboratory and field tests to provide the specialized photointerpretive data necessary to more precisely evaluate the encounter photographs.

The original proposal to do TV photography of local terrain from elevated ground sites and/or aircraft was discarded in favor of laboratory studies as the magnitude of the problem was more fully understood. The pre-encounter activities were divided into five general categories:

- (1) A TV subsystem was selected that could closely simulate the flight subsystem (S/N MC-4) in sensitivity, color response, and geometric characteristics. The subsystem selected was a hybrid consisting of electronics from the prototype system and a proof-test-model (PTM) camera head of an early mechanical design with especially selected vidicon tube and color filters of the flight type. This subsystem (S/N P-2) exhibits response characteristics within a few percent of those of the flight subsystem (Fig. 4).
- (2) Laboratory tests will be performed to determine detectability thresholds of simple simulated topographical features (e.g., slopes and edges, characteristic of faults and mountain-forming activities) and variations in color and albedo typical of terrains of differing composition or age lying adjacent. Combinations of both phenomena will also be studied.

Quantitative testing was done with simple step models painted in grey shades to simulate Martian light- and dark-area albedos ( $\rho = 0.18$  and  $0.07$ , respectively). The models were illuminated by collimated light at geometries analogous to those antici-

pated at encounter. A 750-w spot-light beam folded by an 88% reflecting mirror provided the light. The models were mounted on a 3-degree-of-freedom pedestal and oriented to desired positions relative to the TV camera and the light beam (Fig. 5).

Additional subjective evaluation studies were made using U. S. Army Map Service topographical relief maps painted in suitable colors to simulate terrain as seen from high altitudes (Fig. 6).

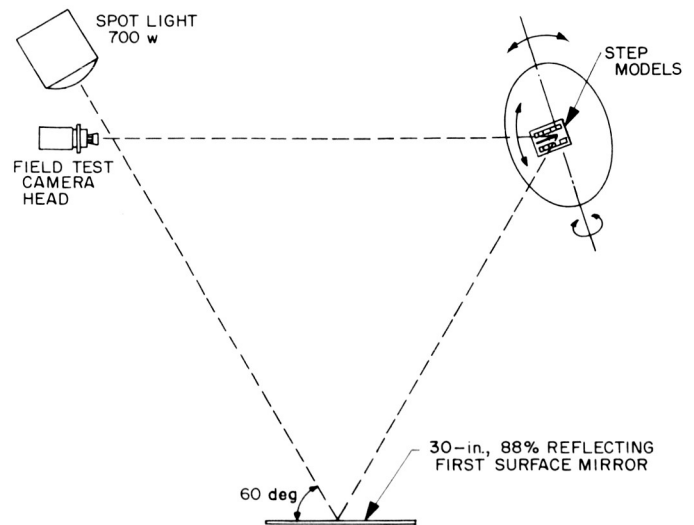


Fig. 5. Laboratory setup for model studies

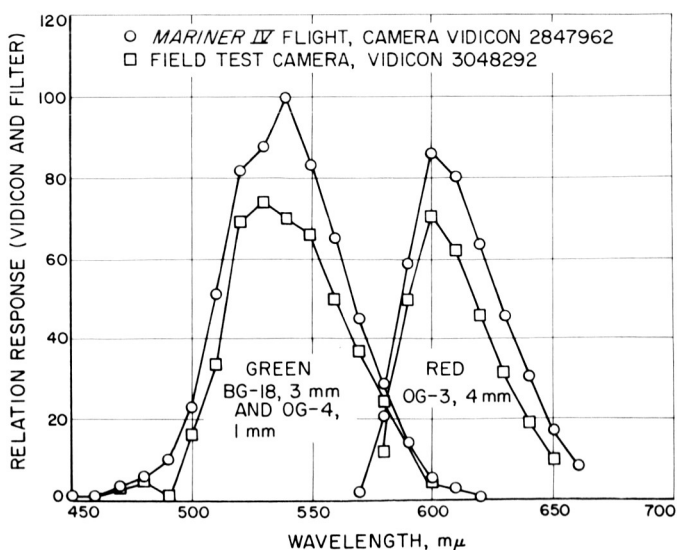


Fig. 4. Spectral response of flight and field-test TV camera systems

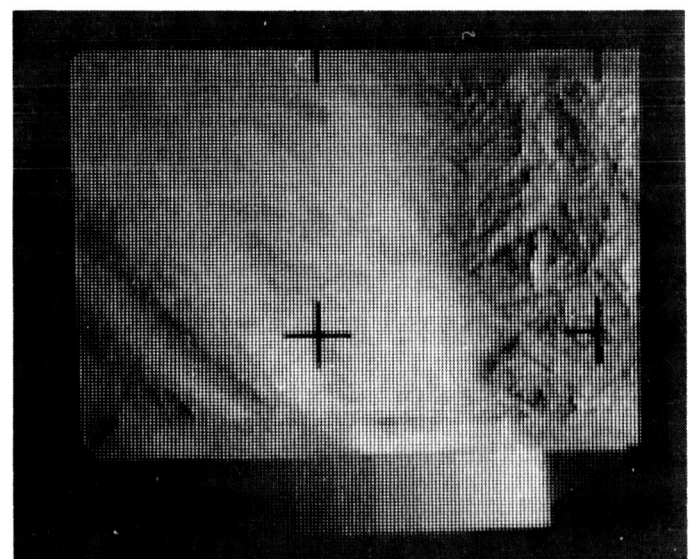
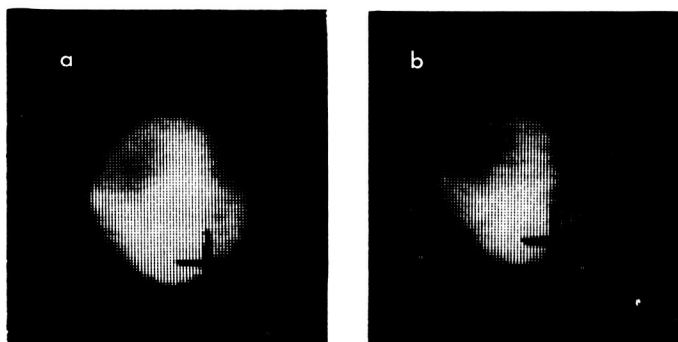


Fig. 6. Terrain model of the Bakersfield, California area (also shown is the linear grey step chart providing a check of system gamma during model studies)



- (3) Field operations at the Mt. Wilson Observatory took place during the March 1965 opposition in order that the sensitivity settings and the color filter selections might be checked by photography of the actual planet. The TV subsystem was coupled to a photometer scanner on the 60-in. telescope in a folded Cassegrain configuration, and direct TV photos were taken of Mars. To compensate for the difference in optics (the flight telescope is a 12-in. focal length telescope, T/8; the 60-in. telescope Cassegrain focus is f/22), variable exposure time was added to the TV and most pictures were taken at 800 msec. On the nights of March 19 and 20, 1965, when reasonable seeing (4 to 6) and very good atmospheric transparency were experienced, more than 60 pictures of Mars (Fig. 7) were obtained, and the video signals were recorded on magnetic tape. Subsequently, the data were digitized and played back into the PDP-4 (Programmed Data Processor 4) computer, and 35-mm negatives were obtained from the Link video processor for analysis.



**Fig. 7. Mars as viewed from Mt. Wilson**  
(a) with green filter, (b) with red filter

- (4) Optimized data and picture processing techniques will be employed. Encounter pictures will be received in 6-bit digital form. After being decoded by a computer, these will be processed by the Link recorder at the telemetry processing station onto 35-mm film. The film is exposed by a cathode-ray tube (CRT) beam that is intensity-modulated by a voltage proportional to the digital level as it scans a 200- $\times$  200-element format.

Laboratory and field test TV picture data are recorded on magnetic tape and by a Flight Research Corporation time lapse cinerecording of the TV monitor display. The magnetic tape data are digitized during playback and, after suitable computer

conditioning, are processed by the telemetry processing station Link system in the same manner as spacecraft data.

To enhance the interpretability of encounter pictures, various parameters of the Link system operation and the computer processing have been varied. The basic 200- $\times$  200-element raster leaves large spaces between dots on the picture [Fig. 8(a)]. To provide a smoother appearing picture, the raster size was decreased, and the dots (CRT electron beam) defocused slightly. Additional fill-in will be accomplished by polynomial interpolation between picture elements to expand the picture to a 400- $\times$  400-element raster. To ensure that all of the data in the picture can be seen, the computer can invert all data so that the Link system may operate in a

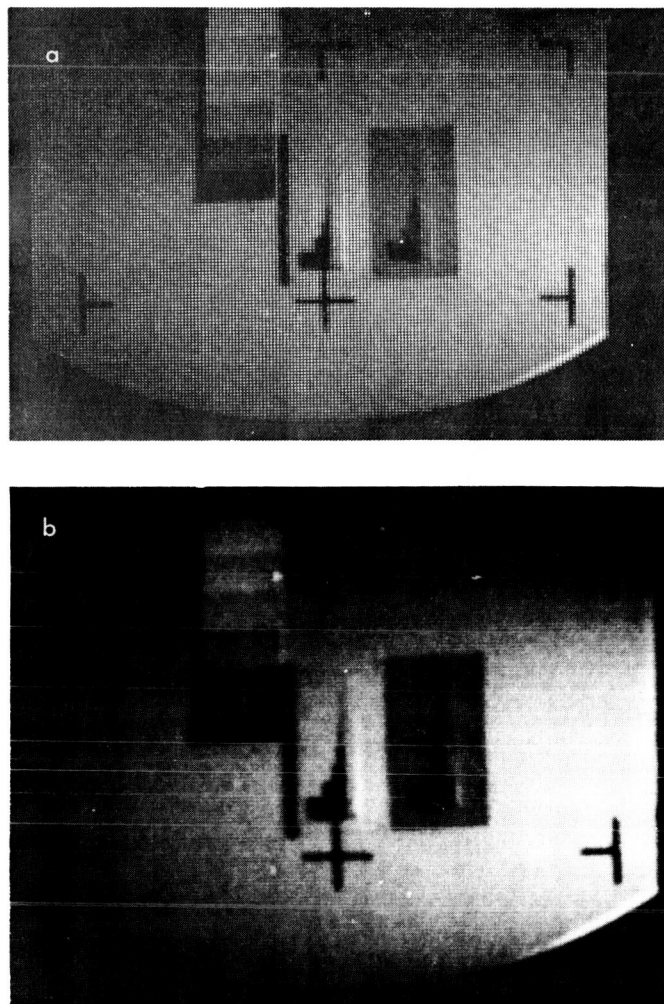


**Fig. 8. Link-system-processed model study picture**  
(a) normal operation, (b) operation optimized to Mariner TV operational parameters

more linear region, and the Link gamma will be adjusted to provide a lower but more linear brightness spread (i.e.,  $\gamma = 1.0$ , cf.  $\gamma = 1.5$ ). The result is a picture showing the scene as photographed, that is, as continuous data without loss of the information between dots as found with the original processing technique [Fig. 8(b)].

- (5) JPL Public Information Office (PIO) activities consisted of providing, for PIO release, *Mariner* TV camera pictures of photographs taken by the *Tiros* and *Ranger* spacecraft. Additionally, pictures of a topographical map of Southern California were taken. In each case, resolution of features in the pictures was arranged to approximate a *Mariner IV* view at the flyby distances predicted for encounter.

Subsequent to encounter, it is anticipated that the model studies will continue to further refine the interpretation of the TV pictures of Mars. Planning is proceeding toward data synthesis in the opposite direction to that previously used; i.e., based on observed data, models will be fabricated and photographed in an attempt to simulate Martian surface phenomena. If portable instrumentation is available, particularly magnetic tape recording equipment, aerial surveys will be conducted to try to match terrestrial surface formations and rock and soil materials to those observed on Mars.

## D. Spurious TV Image Phenomena

### 1. Introduction

A brief study has been made of a spurious image phenomena that arose in the latter stages of the development of the *Mariner* TV camera head. The general appearance of the phenomena is illustrated in Fig. 9, where it will be noted that a dark line appears at the top of the picture.

The spurious line first became evident when a revised optics assembly required readjustment of the vidicon focus position. The cause was determined to be interaction of the shutter solenoid field with the vidicon photoconductor. Fig. 10 is a photograph of the front end assembly showing the relative positions of the solenoid and vidicon. Additional shielding would eliminate the problem; however, the image defect was not sufficiently adverse to warrant possible schedule delays for implementing reliable shielding hardware.

There are two possible explanations for the origin of the line. The first assumes that it is a position phenomena that corresponds to a particular orientation of the solenoid magnetic field. The second assumes that it is a time phenomena that is related to magnetically induced particle-relaxation times in the semiconductor crystal lattice.

### 2. Vidicon Operation

Before discussing either possibility, the operation of the slow-scan vidicon will be described together with certain observations that have been made. Prior to exposure, the vidicon is in an erase-and-prepare mode. During this time, the capacitive component  $\Delta C$  of the picture elements is charged by the scanning beam to the applied target potential. This sets up an electric field normal to the semiconductor surface. Subsequent exposure generates mobile carriers that create a displacement current  $i$  that is oriented by the electric field to discharge the  $\Delta C$  elements. In the read-out mode that starts coincidentally with exposure, the scanning beam replaces the  $\Delta C$  charge to produce the signal current. In *Mariner*, the signal current is an RF-modulated component at 105 kv that is produced by chopping the beam. Two hundred lines are scanned out in a frame period of 24 sec, with an active line time of 14.4 msec and an over-all line time of 120 msec.

### 3. Magnetic-Field Interaction

The exposure is electromechanically timed with a two-pulse open-close shutter action. Two exposure times are provided, 200 and 80 msec, with a drive pulsewidth of 25 msec. Only the trailing edge of the first pulse and the leading edge of the second pulse are included within the optical exposure. Thus, while the photoconductor is illuminated, there are two switched magnetic fields, one in each direction. The spurious line becomes evident during the subsequent read-out period at times which may be 1 or 2 sec later than the exposure time. The pulsed-field magnitude measured in the vicinity of the vidicon faceplate is 2 gauss. The phenomena under discussion is most evident when the exposure operates with the 200-msec pulse spacing as shown in Fig. 9. The effect is less pronounced and occurs earlier in the read-out scan with the 80-msec spacing.

Attempts have been made to create spurious delayed images by introducing into the illuminated photoconductor changing magnetic fields produced by switched solenoids or hand-moved magnets. These are at best only marginally noticeable, probably because of timing difficulties. If the same fields are applied during the later

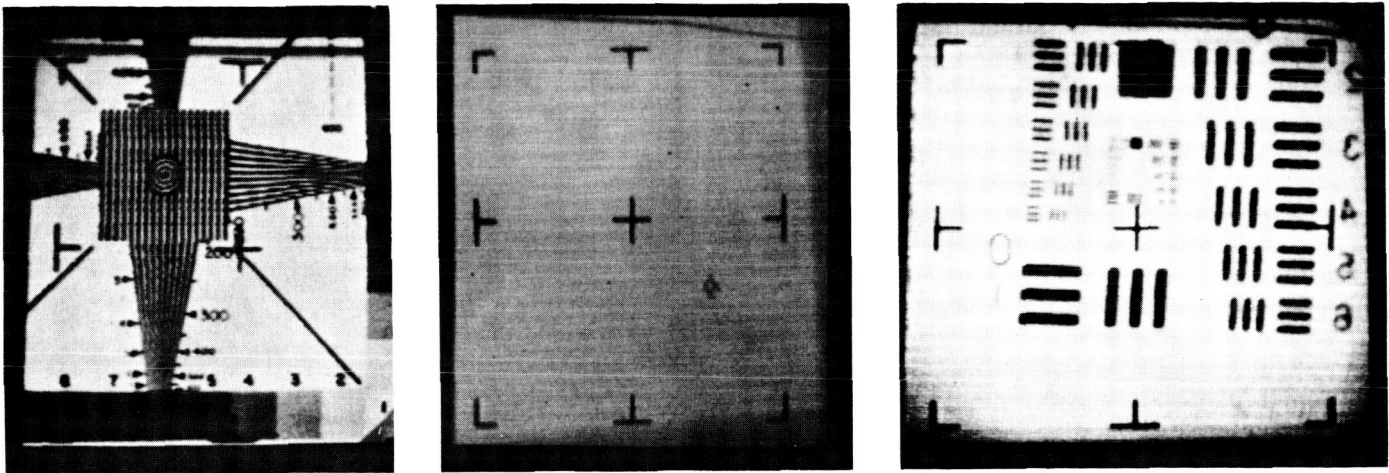


Fig. 9. Spurious line phenomena in *Mariner* TV subsystem

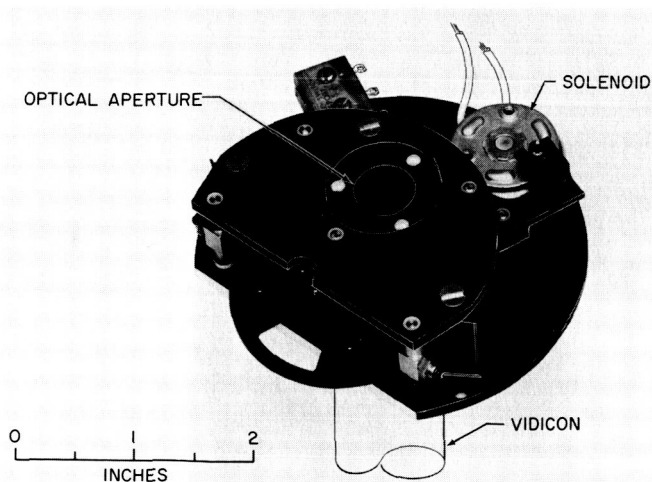


Fig. 10. Camera head shutter assembly

read-out mode, the visible effect produced occurs only at the instant that signal current is being produced (i.e., Faraday's law).

If the spurious image is to be caused by a positional phenomena, then some critical value and direction of a magnetic-field line must disturb the electrical field in the  $\Delta C$  elements concerned at the time of exposure. Such an event might be produced by the Hall effect.

#### 4. The Hall Effect

In 1879, E. H. Hall discovered that a potential difference arose perpendicular to the direction of current flow when a suitably oriented magnetic field was introduced into a material carrying current. It was not until 1934 that the Hall effect was first noted in photoconductors,

when it was then described as the PEM or photoelectromagnetic effect. The PEM effect is described as follows: If a semiconductor is illuminated and a magnetic field is introduced perpendicular to the direction of illumination, an EMF is induced that is normal to both the photocurrent and the magnetic field.

The relationship between the magnetic field of the solenoid and the photoconductor in the *Mariner* camera head is illustrated in Fig. 11. The coordinates are shown more simply in Fig. 12(a), where  $H$  represents the solenoid field;  $E_x$ , the direction of the electric field across the semiconductor; and  $E_h$ , the field induced by the PEM effect. Illumination is directed along the  $x$ -axis and generates a photocurrent  $i$ .

In accordance with a simplified analysis presented by Bube<sup>1</sup>, the potential that produces  $E_h$  is proportional to the current density  $j$  and the magnetic-field intensity  $H$ , i.e.,

$$\text{Grad } V_h = -h(j \times H) = -hjH = -E_h, \quad (1)$$

where  $h$  is the Hall constant. As shown in Fig. 12(b), the resultant electric field may be regarded as a change in the direction of the original field  $E_x$  operating in the crystal lattice. The change in the direction is the Hall angle,

$$\tan \theta \approx \theta = E_h/E_x = hjH/j/\sigma = Hh\sigma, \quad (2)$$

where  $\sigma$  is the conductivity.

<sup>1</sup>Bube, R. H., *Photoconductivity of Solids*, Chapter 8, John Wiley and Sons, Inc., New York, 1960.

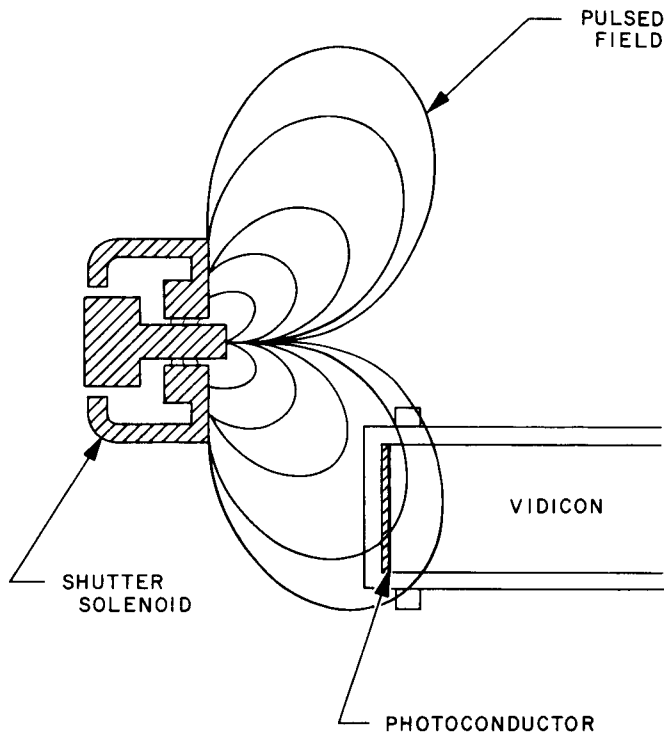


Fig. 11. Relationship of photoconductor to shutter-solenoid field

By considering the magnetic and electric forces acting on the electron in the  $y$ -direction, it can be shown that  $E_h = jH/ne$ , where  $n$  represents the free carriers produced by illumination and  $e$  is the electron charge. Substituting in Eq. (1) the Hall constant  $h = 1/ne$ , the Hall angle  $\theta = H/ne\rho$ , where  $\rho$  is now the target resistivity.

The Hall angle may be determined for the *Mariner* vidicon by considering an elemental picture area  $\Delta A$  and estimating the population  $n$  from the quantum efficiency. A typical value for the *Mariner* vidicon is  $n = 0.44 \times 10^6$  photoelectrons for an illumination  $I_s = 0.01$  ft-c/sec. Taking  $\rho = 0.5 \times 10^{14}$  ohm/cm<sup>3</sup>,

$$h = \frac{1}{0.44 \times 10^6 \times 1.6 \times 10^{-19}} = 1.4 \times 10^{13}.$$

The Hall angle

$$\theta = \frac{1.4 \times 10^{13} \times 2.0}{0.5 \times 10^{14}} = 0.56 \text{ rad} = 32 \text{ deg}$$

for a measured solenoid field at the photoconductor  $H = 2$  gauss.

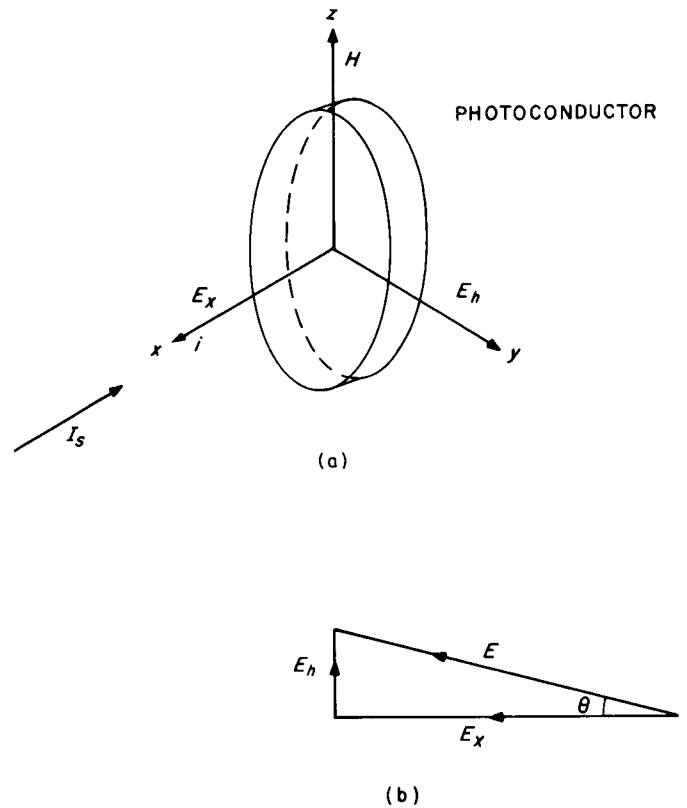


Fig. 12. Reorientation of the electric field across the crystal lattice with an added magnetic field

This brief analysis appears to indicate that the magnitude of the solenoid field is sufficient to produce appreciable disorientation of the normal electric field across a  $\Delta C$  element.

## 5. Spin Resonance

Considering next a time phenomena as the origin of the spurious image, a disturbance in the photoconductor crystal lattice that is produced in the time domain requires a relaxation phenomena of an oscillatory form in order to meet the nature of the observed line image, which, when sloped, appears and disappears on succeeding lines. This might be expected from nuclear particle spin resonance activated by a fast-changing magnetic field operating in the presence of an RF current, the 105-kc beam-current component.

The energy equation for nuclear resonance is

$$h\nu = g_i B_N H, \quad (3)$$

where  $h = 6.6 \times 10^{-27}$  ergs/sec,  $\nu$  is the RF frequency,  $B_N$  is the nuclear magneton, and  $g_i$  is a factor related

to the gyromagnetic ratio. For proton resonance,  $H = 2.35 \times 10^{-4} \nu$ ; so, for  $\nu = 105$  kc,  $H = 25$  gauss, which is much higher than the field measured.

Similarly, for electron resonance,

$$h\nu = gBH, \quad (4)$$

from which  $H = 3.57 \times 10^{-7} \nu$ ; for  $\nu = 105$  kc,  $H = 0.04$  gauss, which is much lower than the measured field.

Electron spin resonance has been studied in semiconductors, but relaxation times are extremely fast. Nuclear-resonance relaxation times, on the other hand, are of the

order of that experienced during the vidicon readout time, 1 sec or longer. It is possible that an oscillatory nature to the spin resonance would be observed on a sensitive system such as represented by the *Mariner* camera system while remaining unnoticed by previous experimenters.

## 6. Conclusion

Of the two possible causes of the phenomena which were investigated, the Hall effect seems to be the more likely origin of the spurious line. The Hall voltage depends inversely on the number of carriers and the thickness of the semiconductor. The slow-scan vidicon photoconductor is only a few microns thick, and the displacement current is only a few nanoamperes.

## VII. Space Instrument Systems

### A. Space Sciences Encounter Planning Activities

#### 1. Introduction

Space sciences personnel have been preparing for the *Mariner IV* encounter with Mars. In early-May 1965, an encounter planning group, staffed by cognizant project personnel from the space sciences analysis and command (SSAC) group and chaired by the division project representative, was created to define division requirements in encounter operations, establish tasks to meet such requirements, and appoint cognizant persons to perform the tasks. The group supports the project encounter preparations working group (EPWG) chaired by the spacecraft project engineer, refines the broader requirements of the EPWG, and translates these requirements to a detailed division effort.

In support of these groups, specialized auxiliary monitoring equipment has been installed in the JPL Space Flight Operations Facility (SFOF); personnel have participated in encounter preparation tests at the SFOF and the JPL Spacecraft Assembly Facility (SAF) as well as in special subsystem tests.

#### 2. SSAC Encounter Planning Group

The group is divided into three subgroups and an SSAC council which acts in an advisory capacity. The three subgroups are: (1) the cognizant engineers, scientists, and investigators associated with the cosmic ray telescope, cosmic dust detector, trapped radiation detector, ionization chamber, plasma probe, and magnetometer; (2) science subsystem project personnel plus the cognizant scientists associated with the data automation system (DAS), scan subsystem, and TV subsystem; and (3) science data support personnel. These groups are directed by the assistant project scientist, project engineer, and science data coordinator, respectively. Each subgroup has been appropriately staffed, and individual tasks have been assigned.

The first subgroup established the facilities required (during encounter) by the personnel working with the assistant project scientist. It is also studying the probable Martian environment in order to predict the occurrence of planet-induced phenomena. This information will aid the spacecraft performance analysis and command group in predicting and analyzing the performance of other spacecraft subsystems. To support the analysis of cruise instrument data in near-real time, computer programs

have been specified. Most of the programs were already in existence and have been utilized throughout the mission for non-real-time analysis.

The second subgroup, directed by the project engineer, has similarly established its needs for facilities. One of these is the installation of equipment for direct on-line processing of the real-time telemetry. This equipment bypasses the usual facility computer processing and provides a means for receiving immediate indications of spacecraft events such as planet acquisition by the wide- and narrow-angle sensors and the TV instrument. Having this information several minutes before it is available on the standard output devices reduces reaction time during this most critical phase of the mission. This equipment also provides a readily interpretable display of all other science data and can therefore be used for real-time science analysis in the event of failures in the primary data processing equipment. The equipment has been installed and was used during two preparedness tests with excellent results.

Members of the second subgroup are also responsible for computing times for the transmission of various commands both in the nominal sequence and in nonstandard sequences. To aid in this, several special computer programs are required, such as time versus DAS frame count and planet scan subsystem data as functions of time. During encounter operations, the time versus DAS frame count program will be run as often as necessary to eliminate the possibility for error. During recent tests, it was shown that the program output could be in the user's hands within 10 min after the request. Additional recent activities of this subgroup are the generation of nominal

expected parameter values of TV and scan subsystem functions. The information was derived from extensive controlled-environment tests of models of these instruments.

The third subgroup, the data handling subgroup, is responsible for seeing that computer programs are written, tested, and implemented and that all output data are distributed expeditiously. To this end, procedures have been established outlining the requirements of the users and the proposed methods of meeting these requirements. One program, the special scan program, predicts the motion of the scan platform on the basis of received real-time telemetry as input, and it outputs a time to send the inhibit command such that the platform attains the proper clock angle for the TV trace. If the command is not sent, the program output is used in conjunction with another program to predict the intercept point on the planet limb for both a searching and tracking scan subsystem. The program is expected to be ready for test during the next reporting period. In addition to these user programs, simulated data on magnetic tapes have been prepared for use in program checkout and personnel training.

### **3. Other Activities**

Tests have been performed on the proof-test-model (PTM) spacecraft and on available spare instruments involving the DAS, scan subsystem, and TV subsystem to answer specific questions on the encounter sequence. To date, three full-scale encounter tests, one in simulated real time covering 26 hr and two scan positioning tests, have been performed in preparation for encounter.